Fall 12-2018

Three-Dimensional Bedrock Channel Evolution with Smoothed Particle Hydrodynamics

Nick Richmond
University of Maine, nicholas.richmond@maine.edu

THREE-DIMENSIONAL BEDROCK CHANNEL EVOLUTION WITH SMOOTHED PARTICLE HYDRODYNAMICS

By

Nick Richmond

B.S. University of Maine, 2015

A THESIS

Submitted in Partial Fulfillment of the

Requirements for the Degree of

Master of Science

(in Earth Sciences)

The Graduate School

The University of Maine

December 2018

Advisory Committee:

Peter Koons, Professor of Earth and Climate Sciences, Advisor

Sean Smith, Professor of Earth and Climate Sciences

Samuel G. Roy, Post-Doctoral Fellow, Mitchell Center for Sustainability Solutions

THREE-DIMENSIONAL BEDROCK CHANNEL EVOLUTION

WITH SMOOTHED PARTICLE HYDRODYNAMICS

By Nick Richmond

Thesis Advisor: Dr. Peter Koons

An Abstract of the Thesis Presented
in Partial Fulfillment of the Requirements for the
Degree of Master of Science
(in Earth Sciences)
December 2018

Bedrock channels are responsible for balancing and communicating tectonic and climatic signals across landscapes, but it is difficult and dangerous to observe and measure the flows responsible for removing weakly-attached blocks of bedrock from the channel boundary. Consequently, quantitative descriptions of the dynamics of bedrock removal are scarce. Detailed numerical simulation of violent flows in three dimensions has been historically challenging due to technological limitations, but advances in computational fluid dynamics aided by high-performance computing have made it practical to generate approximate solutions to the governing equations of fluid dynamics. From these numerical solutions we gain detailed knowledge of the motions and forces of flowing water, which deepens our understanding of earth processes responsible for shaping landscapes.

By simulating hydraulic forces generated by flowing water in bedrock channels with interconnected zones of weakness, I explore the implications of fluvial stresses, boulder impact, and rock fabric heterogeneity on landscape form. I use a Smoothed Particle Hydrodynamics (SPH) solver to simulate flow over landscapes and I use stress-strength analysis to calculate earth

fabric failure using the Failure Earth Response Model (FERM). SPH modeling is used to simulate the hydraulic mobilization of a boulder in a bedrock channel and to quantify the forces associated with its subsequent rolling, sliding, and impact two-meter freefall. FERM model results reveal that strength gradients in fractured bedrock topographies exert more control on volume of eroded material and channel form than the overall strength of the surrounding bedrock.

Finally, SPH model results are calibrated with three-dimensional water velocity measurements collected by an acoustic doppler current profiler in the Penobscot River. SPH modeling is used to explore the influence of in-stream logging structures on channel velocity, which has implications for the habitat of federally-protected diadromous fish species in the Penobscot River. Model results show that even at low discharges, the presence of in-stream structures changes the velocity structure at ~10^2 m length scales.

DEDICATION

This thesis is dedicated to Kate Huntress and Anthony Richmond, whose constant reassurances that everything would work out just fine, made everything work out just fine.

ACKNOWLEDGEMENTS

I owe the utmost gratitude my advisor, Dr. Peter Koons, who at every turn provided the support, guidance, and creativity needed to craft and execute my research project. Whether at the whiteboard or on the river, Dr. Sean Smith was tremendously helpful with all aspects of bridging the gap between my numerical modeling work and local applications with interdisciplinary connections. Dr. Sam Roy gave me the gift of his time even when it was a scarce commodity, and I am enormously grateful for all the thoughtful discussions and thorough feedback that helped me turn ephemeral ideas into actionable research. During my undergraduate studies, it was Sam who first introduced me to the magic of numerical modeling, and I would have never made it this far without his kindness and inspiration.

Dr. Phaedra Upton has been instrumental to my understanding of how the earth works, and despite being 18 hours ahead and 12,500 km away, was astoundingly willing to help me troubleshoot tricky problems. I am deeply grateful to the DualSPHysics development team for their encouragement and support on conceptual and practical levels. Without their tireless commitment to producing cutting-edge research tools and supporting those who use them, this project would have been unlikely to get off the ground. Dr. Lauren Ross and Dr. Joe Zydlewski were crucial to accomplishing the field work component of my research. I am very thankful to Dr. Chris Gerbi and Dr. Kat Allen for offering me engaging work which broadened my perspective of the Earth Sciences. I owe much to the denizens of the Geodynamics Research Group, who helped me process my ideas and inspired me with their own.

I would like to acknowledge the support from the National Science Foundation (including GeoPRISMS OCE-1249909 and EPSCoR #7552151), New England Sustainability Consortium, Maine Agricultural and Forest Experiment Station, Climate Change Institute, UMaine Graduate

Student Government, and UMaine School of Earth and Climate Sciences for supporting my research initiatives.

Lastly, I would like to extend my heartfelt thanks to the friends and family who enriched my life outside of UMaine, and to Jean Koons of Kennebec Cheesery for the generous helpings of chèvre that put an extra spring in my step.

TABLE OF CONTENTS

LIST OF TABLES

LIST OF FIGURES

LIST OF EQUATIONS

CHAPTER 1

KINEMATICS AND DYNAMICS OF BEDROCK CHANNELS

Introduction

By incising into bedrock and transporting material away from uplifted terrains, bedrock channels are responsible for balancing and communicating tectonic and climatic signals across landscapes. For this reason, bedrock channels are well-studied in the fields of quantitative geomorphology and landscape evolution. Over 10^1-10^3 year timescales, bedrock channels tend to transport more sediment than supplied and typically have little-to-no alluvial cover, which makes the bounding rock susceptible to plucking, abrasion, cavitation, and other destructive processes (Whipple et al., 2000, 2013). Fluvial erosion in bedrock channels is typically calculated with the assumption of steady uniform flow as a function of cross section averaged bed shear stress τ:

$$\tau = \rho g^{2/3} C_f^{1/3} Q^{2/3} S^{2/3} \quad 1.1$$

where ρ is the fluid density, g is gravity, C_f is a dimensionless friction coefficient, Q is discharge, and S is local slope.

The scalar local bed shear stress τ, which is averaged over a flow-perpendicular cross-section to approximate the stresses associated with water flowing past bedrock, greatly simplifies the dynamics of fluid-structure interaction. In nature, the forces created from water flow in a channel are three-dimensional, requiring that quantification of the total stress as a second-order tensor. Expressing the stress as a horizontally-averaged scalar value ignores stress gradients along the horizontal plane and discounts the role of stresses arising from forces in any direction other than downstream parallel with overall channel longitudinal profile. In the case of flows with appreciable forces acting perpendicular to the mean flow direction, such as in the case of sharp

river bends or steep plunges, the scalar treatment of horizontally-averaged local bed shear stress will necessarily fail to capture the stresses produced by the application of 3D forces.

The loss of detail that arises from relying on a horizontally-averaged scalar shear stress value to approximate the work done by flowing water on the surrounding landscape begs the question, why not instead use a first-principles approach grounded in the physics of flowing water? To do so would require using the governing equations of the motions of incompressible fluids, the Navier-Stokes (N-S) equations:

$$\rho \frac{\partial v}{\partial t} = -\nabla P + \Delta g h + \mu \nabla^2 v \qquad 1.2$$

where ρ is fluid density, v is velocity, t is time, P is pressure, g is gravity, h is height of the fluid column, and μ is dynamic viscosity. It is computationally expensive to generate approximate solutions to the N-S equations and their vertically-averaged counterpart, the Shallow Water Equations (SWE), which has historically made it impossible or impractical to solve for flow using first principles. The tendency of channelized flows to accelerate slowly at the reach scale has been used as justification for simplifying the treatment of flowing water in landscape evolution models and thus avoiding the computational expense of solutions to the SWE or N-S equations (Tucker and Hancock, 2010; Temme et al., 2017). This is justifiable for models operating at the mesoscale, or 10^0–10^2 km and 10^1–10^3 years (Brasington and Richards, 2007), which is true for most landscape evolution models. For models which use a microscale spatial domain (less than 10^2 km) but operate at timescales ranging from hours to years, the use of empirical relations to constrain fluid-structure interaction is logical in cases where at least one spatial dimension is negligible or easily parameterized within the problem domain (e.g., Liao et al., 2014; Scheingross and Lamb, 2017).

For problem domains that have a strong dependence on high-Re complex flows over irregular 3D shapes, a physics-based approach provides deeper insights into the dynamics of the bedrock channel system. Quarrying of bedrock blocks during extreme discharge events is a primary erosion process in bedrock channels, especially in environments where exposed fractures, joints, and bedding planes dominate (Whipple et al., 2000). Large erosional events are difficult and often dangerous to observe in nature (Lamb et al., 2015), which makes analog and numerical modeling practical approaches to investigating phenomena such as block quarrying. Dubinski and Wohl (2013) used high-Re flow past a series of cement blocks in a flume to examine the quarrying action of hydraulic forces on blocks in a heavily-jointed bedrock channel with steps and knickpoints. Although physical quantities such as pressure exerted on blocks in the flume are framed in terms of empirical relations to scalar bed shear stress, the role of 3D geometry and normal forces is used to describe block sliding at the knickpoint, a mode of removal not described by previous geomorphological studies framed in one or two-dimensional physics.

Flume experiments performed by George and Sitar (2015) show that channel block entrainment has a strong dependence on the 3D orientation and geometry of channel blocks, which in turn implies that the 3D orientation of the flow field is important to channel block failure. In the flume experiments, a tetrahedral block fitted with pressure sensors for hydraulic load measurement and proximity sensors for displacement measurement provided detailed 3D kinematic information about the lifting, sliding, and rotation of the block in a series of high-Re flow conditions. Collecting even more detailed information about the hydraulic forces involved in bedrock channel evolution is inherently difficult in analog experiments due to the practical limits of instrumentation. This presents an opportunity to use 3D numerical modeling to provide detailed information about the kinematics and dynamics of a bedrock channel throughout the

model domain, which requires a 3D flow solver capable of providing efficient approximations of the Navier-Stokes equations.

In summary, detailed descriptions of the physics of bedrock channel erosional mechanisms rely on detailed knowledge of the kinematics and dynamics of flow in bedrock channels. While the need for increasing detail and dimensionality has been recognized by the community, the dense information fields provided by 3D numerical simulation of hydraulic forces have been historically out of reach due to technological limitations. With the advent of numerical methods accelerated by high performance computing (HPC), the detailed simulation of hydraulic forces in bedrock channels is within reach. This chapter will focus on the application of HPC-accelerated computational fluid dynamics solutions to bedrock channel flows to quantify the forces associated with hydraulic action and boulder impact on the channel boundary.

Methods

Smoothed Particle Hydrodynamics Formulation

Smoothed Particle Hydrodynamics (SPH) is a Lagrangian meshless numerical method for approximating the physics of fluid behavior by representing a fluid continuum as a series of particles. Each particle is a computational node representing physical properties such as position, velocity, density, and pressure. Particle motions depend on the values of these physical properties updated at every time step. The physical properties of any given particle in the continuum are approximated through interpolation using a smoothing kernel that produces a smoothed field of physical properties throughout the fluid continuum. The kernel provides a weighted sum of the physical properties of nearby particles such that the properties of any given particle are most influenced by its closest neighbor particles (Figure 1.1).

Figure 1.1 – Components of the SPH Smoothing Kernel *(after Pringgana, 2016)*

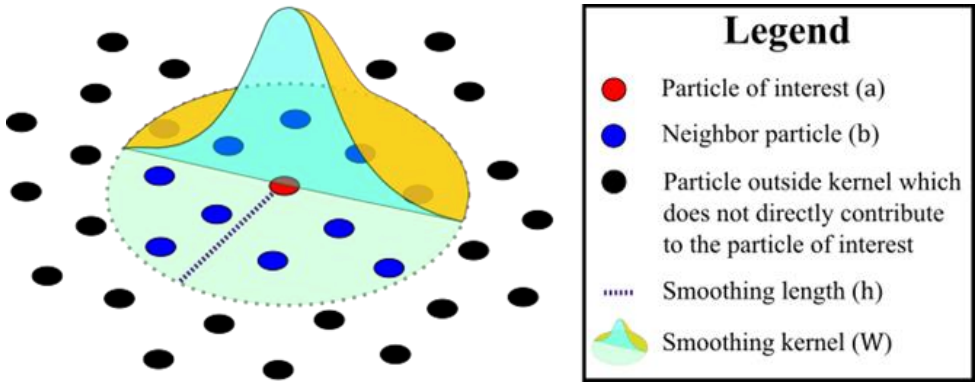

The weight assigned to the interpolation points within the smoothing kernel is shown here as the height of the smoothing kernel.

The smoothing length, which is the radius of the kernel function, defines the zone of influence within which neighbor particles affect the physical properties of any given particle. Any property of a particle with position is approximated in accordance with the conservation laws of continuum mechanics using the integral interpolant $F(\mathbf{r})$:

$$F(\boldsymbol{r}) = \int_{\Omega} F(\boldsymbol{r}')W(\boldsymbol{r} - \boldsymbol{r}', h)d\boldsymbol{r}' \tag{1.3}$$

where W is the kernel function, h is the smoothing length, Ω is the interpolation space, r is the position of the particle, and r' is the position of another particle within the smoothing kernel. The smoothing kernel W must have the following properties (Monaghan, 2005):

- Positive inside zone of particle interaction

$$W(\boldsymbol{r}, h) > 0 \tag{1.4}$$

- Symmetric

$$W(\boldsymbol{r}, h) = W(-\boldsymbol{r}, h) \tag{1.5}$$

- Normalized

$$\int_{\Omega} W(\boldsymbol{r}, h)d\boldsymbol{r}' = 1 \tag{1.6}$$

- Approximates Dirac delta function as $h \to 0$

$$\lim_{h \to 0} W(\boldsymbol{r}, h) = \delta(\boldsymbol{r}) \tag{1.7}$$

- Provides compact support (vanish at a finite distance)
- Differentiable

By using a second order differentiable smoothing kernel, the gradient and Laplacian of $F(\boldsymbol{r})$ are determined by the following differentiated forms of the integral interpolant, where for all neighbor particles b that fall within distance h of particle of interest a:

(Gradient)
$$\nabla F(\boldsymbol{r}) = \sum_{b} F_b \frac{m_b}{\rho_b} \nabla W(\boldsymbol{r} - \boldsymbol{r}_b, h) \tag{1.8}$$

(Laplacian)
$$\nabla^2 F(\boldsymbol{r}) = \sum_b F_b \frac{m_b}{\rho_b} \nabla^2 W(\boldsymbol{r} - \boldsymbol{r}_b, h) \tag{1.9}$$

Differentiation of the kernel provides access to derivative properties of any physical property held by the particles. The use of a smoothing kernel allows for efficient approximation of the fundamental equations of fluid dynamics. Consider the Navier-Stokes acceleration equation (with gravity):

$$\rho \frac{\partial \vec{v}}{\partial t} = -\nabla P + \mu \nabla^2 \vec{v} + \rho g \tag{1.10}$$

In SPH notation, the Navier-Stokes acceleration equation is:

$$\frac{dv_a}{dt} = -\sum_b m_b \left(\left(\frac{P_a}{\rho_a^2} + \frac{P_b}{\rho_b^2} \right) + \Pi_{ab} \right) \nabla_a W(\boldsymbol{r}_a - \boldsymbol{r}_b) + g \tag{1.11}$$

where Π_{ab} is an artificial viscosity term that accommodates shocks to the fluid and promotes numerical stability (Monaghan, 2005).

SPH convention for simulating behavior of low-viscosity liquids is to assume weak compressibility, where density fluctuations in the fluid must be less than 1% (Monaghan, 2005; Crespo et al., 2015). Since the mass of particles is held constant in an SPH simulation, density fluctuations are calculated using the Continuity Equation:

$$\frac{d\rho_a}{dt} = \sum_b m_b v_{ab} \cdot \nabla_a W_{ab} \tag{1.12}$$

Among the variety of methods for handling the interaction of fluid and boundary objects, the computationally inexpensive convention is to represent immovable boundary objects as lattices of fixed particles. As fluid moves past the fixed boundary particles, the zero velocity of the boundary particles approximates a no-slip boundary condition (Crespo et al., 2007). The forces

exerted on a boundary particle by all fluid particles b falling within the zone of particle interaction is calculated as follows (Barreiro et al., 2013):

$$F_{total} = -m_b \sum_b \frac{dv_k}{dt} \quad 1.13$$

In summary, SPH is an interpolation method that uses the physical properties carried by particles in a continuum to approximate the kinematics and dynamics of a fluid in motion. By calculating the motions of individual fluid particles without a mesh, the motions of the fluid continuum are calculated efficiently while being able to accommodate high strain rates and complex free-surface dynamics. As such, violent flows characterized by strong accelerations such as jet impact

The SPH solver DualSPHysics (Crespo et al., 2015) was used to perform the hydraulic modeling presented in the Results section. There are many advantages to choosing DualSPHysics, most notably the optimization of the code for GPU parallel processing. Running the DualSPHysics code on a GPU vastly decreases solution times, thereby allowing high-resolution and/or large-domain cases to be executed efficiently. Both DualSPHysics v4.2 and v4.3 Beta were used to produce the model results presented in this chapter. DualSPHysics v4.2 is the second major release of the code to include a utility for computing the forces exerted on boundary objects by fluid-structure and structure-structure interaction. DualSPHysics v4.3 Beta is the first release of the code to introduce inlet-outlet boundary conditions, the formulation for which is described by Tafuni et al. (2018). Open boundary conditions allow explicit definition of the water surface elevation and velocity profile of particles entering or exiting the domain, which is essential to modeling channelized flows.

In addition to fluid-structure interaction with fixed boundary objects, DualSPHysics also provides means for modeling fluid-structure and structure-structure interaction with moving

boundary objects of arbitrary size and shape. While also offering a Distributed Contact Discrete Element Method option (Canelas et al., 2016, 2017), the most sophisticated moving boundary treatment in DualSPHysics v4.3 Beta is provided by the synchronous coupling of DualSPHysics and Project Chrono, a multibody dynamics solver (Mazhar et al., 2013; Brito et al., 2016; Canelas et al., 2018). In this coupling scheme, the differential variational inequality method is used to implement the Coulomb friction model, which resolves the forces between individual solid elements in frictional or collisional contact with one another, enabling simulation of the motions of hundreds or thousands of three-dimensional solid elements. The solid components in the DualSPHysics-Chrono system represent Earth materials by prescribing appropriate density, friction coefficients, and restitution coefficients.

All models presented in the Results use the following SPH parameters: Wendland kernel, artificial viscosity scheme, and a Symplectic time-stepping algorithm. Other important model parameters such as simulated time and interparticle distance are reported on a case-by-case basis. Where possible, the dynamics are reported in terms of traction vector magnitude (force / interparticle distance squared) rather than force to maintain consistency across models with different interparticle distances. The models share the same basic channel geometry with a knickpoint, which was chosen to take advantage of the ability to simulate strong fluid accelerations. The knickpoint case is useful for demonstrating the importance of resolving the inertial term of the N-S equations, which enables solutions to the forces associated with the strong negative acceleration of water as it impacts normal to the channel bottom (Figure 1.4).

Figure 1.2 – Simple Knickpoint Geometry Design

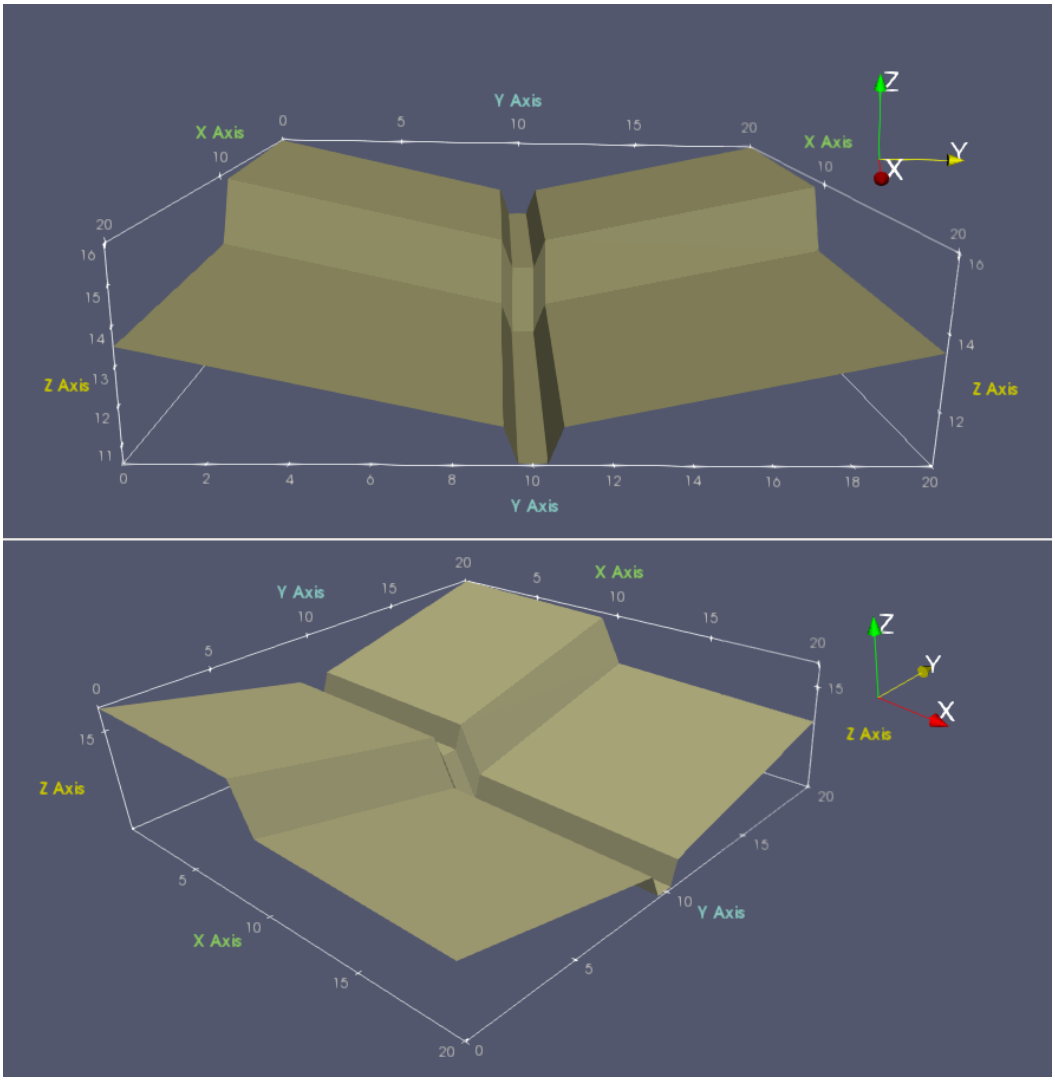

The simple geometry used in the knickpoint model is 20 m long, 20 m wide, with a channel which has a 2° slope behind and ahead of a 2 m drop half-way along the x-axis. This geometry occurs in nature both in knickpoint and fault scarp form (Figure 1.3).

Figure 1.3 – Fault Scarp in the South Island of New Zealand Following the 2016 Kaikoura Earthquake

Though not a knickpoint, the fault scarp pictured above (photo credits: Kate Pedley, University of Canterbury) displays a similar geometry to the synthetic knickpoint shown in Figure 1.2. It is reasonable to expect that overland flow from the surrounding hills might produce a channel which is very similar to the synthetic knickpoint model.

Results

Quantifying Hydraulic Forces

To take advantage of DualSPHysics' ability to simulate 3D flows and their associated forces, I created a simple channel geometry with a knickpoint. The model shown in Figure 1.4 simulates channelized flow past a simple knickpoint with 72,240 particles using an interparticle distance of 10^{-1} m. The channel velocity at the 0.9 m^2 channel inlet was set to 5 m/s, which corresponds to a discharge of 4.5 m^3/s. Flow was modeled for 45 seconds of simulated time. The history of traction vector magnitude shown in Figure 1.5 indicates that the initializing perturbations settle out after ~10 seconds of simulated time.

Figure 1.4 – Kinematics and Dynamics of Flow at a Simple Knickpoint

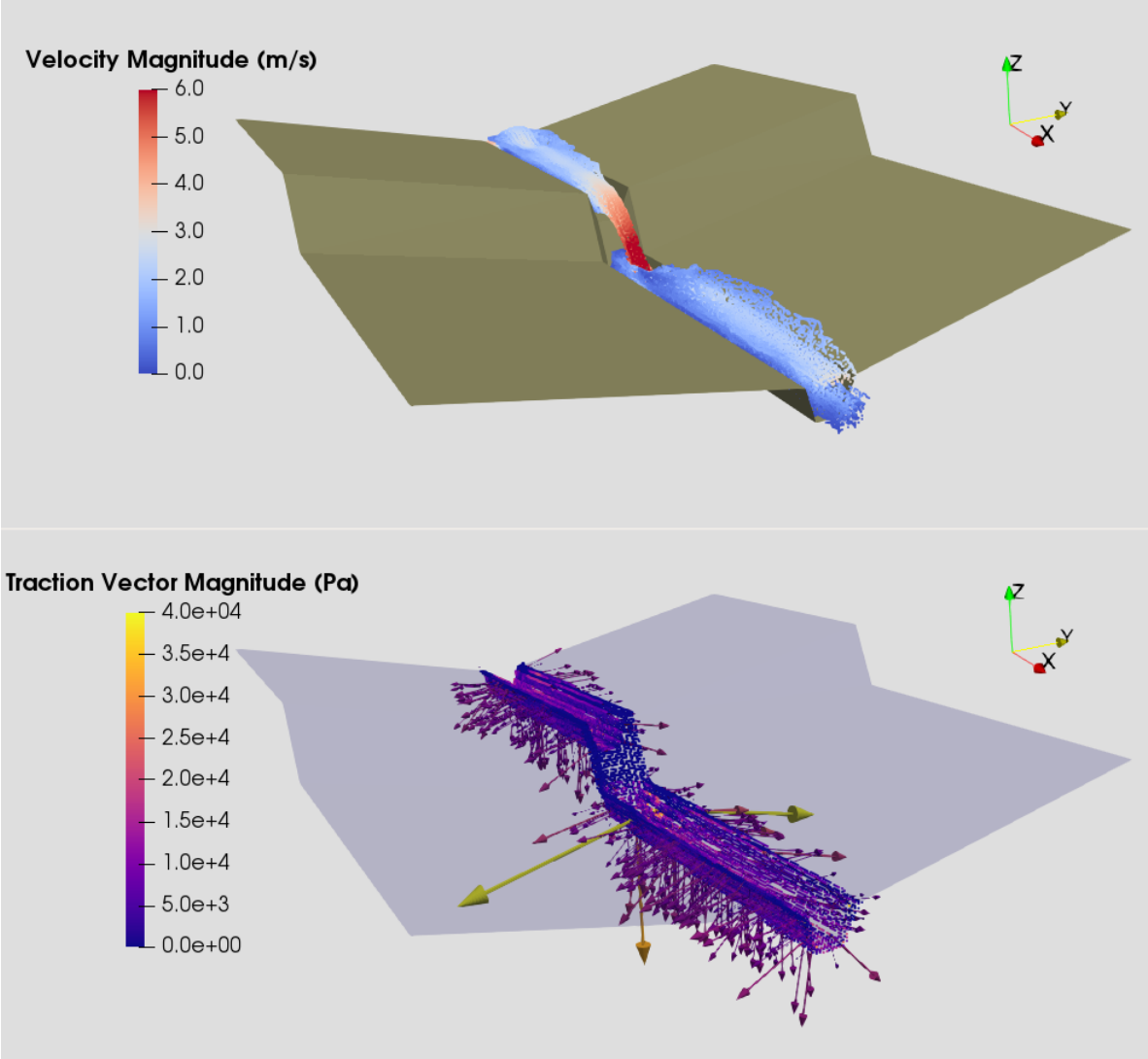

The top frame shows flow velocity magnitude, which exceeds 6 m/s as the stream plunges past the knickpoint. The bottom frame shows the traction vectors (force vector divided by area, which is inter-particle distance squared) associated with the hydraulic forces exerted on the boundary. Note that the forces are highest at the base of the knickpoint which corresponds to the zone of maximum negative acceleration of the fluid, and the strongest forces are both downward and lateral in direction with respect to mean flow direction.

Figure 1.5 – Transient Forces Acting on the Knickpoint Base

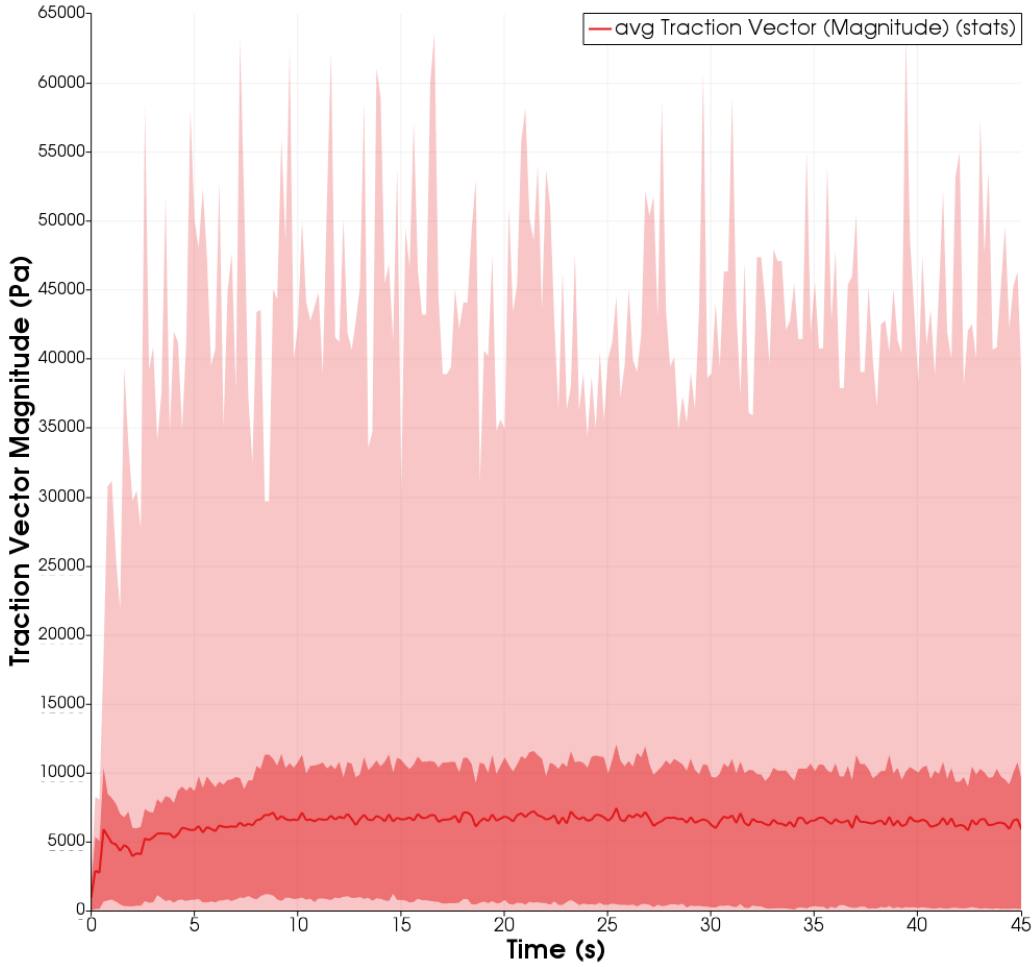

The lightest red data series shows the range of forces acting on the base of the knickpoint in the region of highest negative fluid acceleration. The medium red data series shows the upper/lower quartiles of traction vector magnitude, and the mean traction vector magnitude is displayed with a dark red line.

Quantifying Clastic Impact Forces

The SPH-DVI method implemented using coupled DualSPHysics-Chrono was used to quantify the forces of a boulder impact on the channel boundary. In the interest of model stability, a subset of the knickpoint geometry was modeled at twice the resolution of the model shown in Figure 1.4 because the boulder geometry is best represented by a dense particle lattice. Additional changes include a gradual increase in flow stage and flow velocity to determine the

hydraulic conditions necessary to initiate boulder motion. The top frame of Figure 1.6 shows the conditions just prior to incipient motion of the boulder, which occurs when surface velocity is 0.25 m/s and the water surface elevation is 0.55 m above the channel bed. The physical properties of the boulder which are used in the DVI Coulomb friction calculation are reported in Table 1.1. The forces associated with the weight of the boulder on the channel boundary correspond to a maximum traction vector magnitude is 7000 N/m^2. The forces exerted on the channel boundary just prior to incipient motion correspond to a maximum traction vector magnitude of 30,000 N/m^2. The forces exerted on the channel boundary at the moment of boulder impact at the base of the knickpoint correspond to a maximum traction vector magnitude of 54,000 N/m^2.

Table 1.1 - Physical Properties of the Numerical Boulder

Volume (m^3)	Density (kg/m^3)	Mass (kg)	Young's Modulus (N/m^2)	Poisson Ratio	Restitution Coefficient	Kinetic Friction Coefficient
0.068	2500	170	$8*10^9$	0.2	0.6	0.7

Figure 1.6 – Initiation of Boulder Motion by Channel Flow

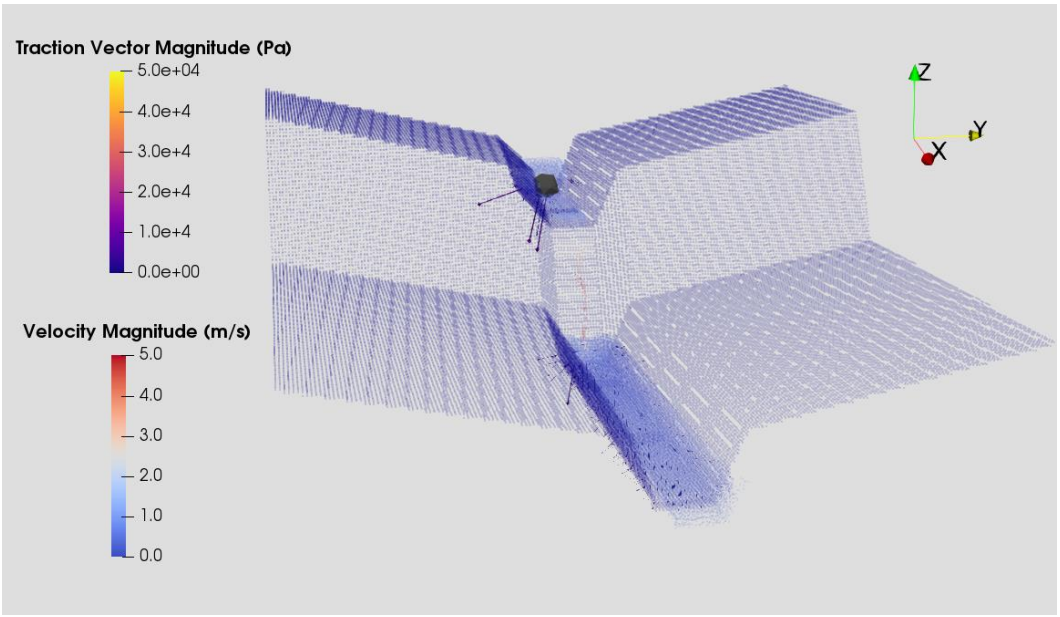

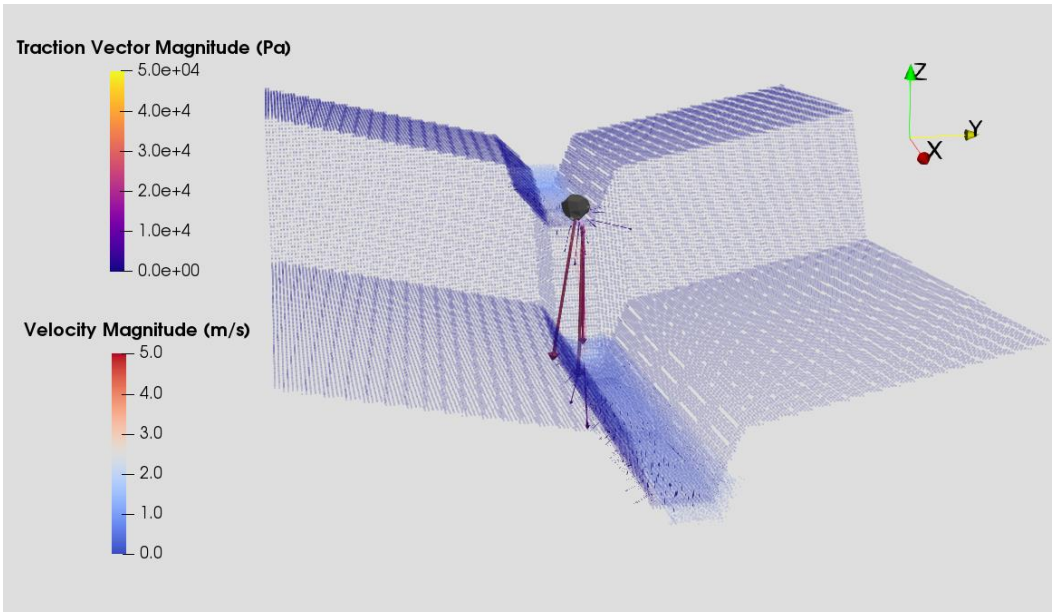

The top frame shows the force (as traction vectors) acting on the channel just before initiation of boulder motion. The bottom frame shows the forces acting on the channel just prior to boulder free-fall off the lip of the knickpoint.

Figure 1.7 – Dynamics of a Clastic Impact

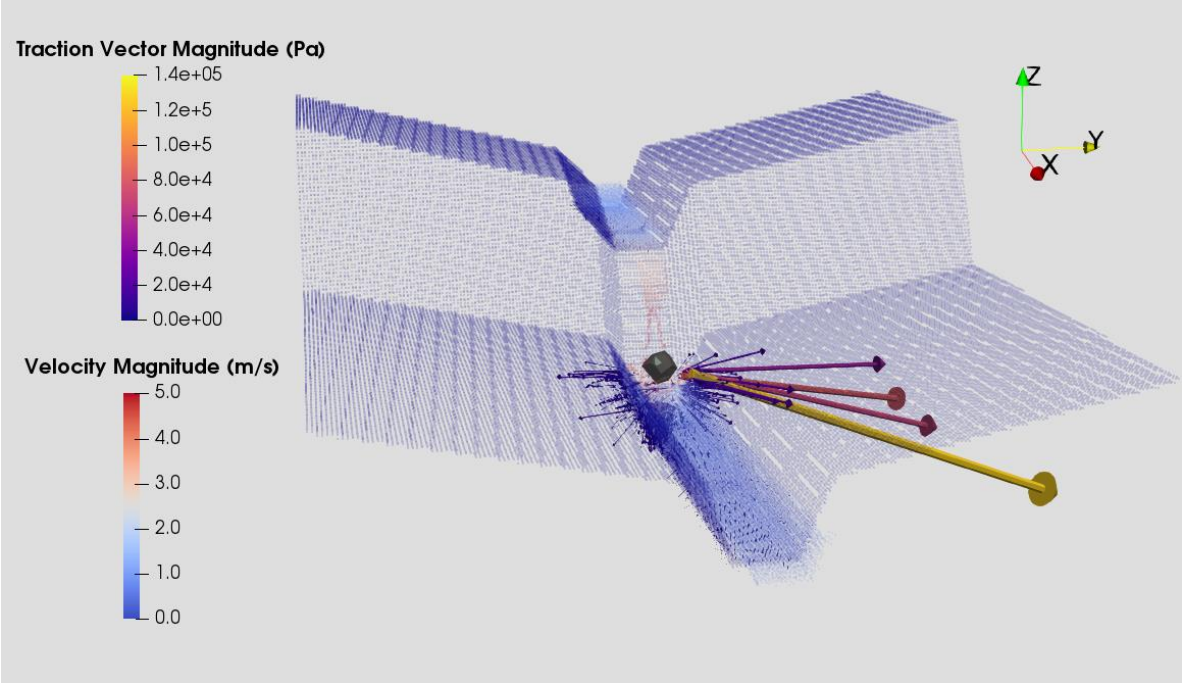

Forces (as traction vectors) acting on the channel at the moment of boulder impact at the base of the knickpoint correspond to a maximum traction vector magnitude of 54,000 N/m^2.

Discussion

The modeled hydraulics presented in this chapter provide detailed information about the connection between the kinematics and associated dynamics of flows characterized by high accelerations. Though lacking in pebble-to-cobble sized sediments to act as erosive tools at the base of the knickpoint, the force distribution shown in Figure 1.4 resembles the dynamics associated with the both the circular jet and radial wall jet at the base of knickpoints as described by Scheingross and Lamb (2017). The high strain rates associated with these jet effects have been historically difficult to model, but the SPH solution provides the forces associated with the jet effects without concern for the mesh violations which plague other numerical methods when simulating violent flows. The transient and variable nature of the forces experienced at the base of the knickpoint (Figure 1.5) suggest that there are dynamic effects associated with differential

pressure acting on, and propagating into, the bedrock below. This is consistent with descriptions of jet-induced scour as described by Bollaert and Schleiss (2003). The presence of transient differential pressures on the bedrock likely has implications with respect to hydrodynamic fracturing and uplift, which are logical avenues of further exploration using the SPH-DVI method afforded by the coupled DualSPHysics-Chrono code.

The exploration of forces associated with hydraulically-driven boulder impact using SPH-DVI yielded compelling quantitative results. Compared to the forces on the channel due to the weight of the boulder, the forces on the channel were four times higher while the boulder was rolling at the lip of the knickpoint and nearly eight times higher at the moment the boulder impacted the bottom section of the channel after its period of freefall over the course of a 2 m vertical drop. In addition to the magnitude of the forces at the moment of boulder impact on the channel bottom, the transient nature of these forces provides further justification for investigating the role of dynamic effects and differential pressures on the fracturing and uplift of material at the channel bottom.

Modeling the motions of cobble-to-boulder sized sediments using SPH-DVI is a clear way to leverage SPH as an investigative tool for entrainment and transport of earth materials. The applicability of SPH to quantitative geomorphology could be further augmented by applying physics-based simulation of particle impacts and the associated damage to bedrock channel boundaries and disruption to unconsolidated sediments. The DualSPHysics solver has already implemented constitutive models for simulation of entrainment and transport of saturated sediments using the Shields and Drucker-Prager criteria (Fourtakas and Rogers, 2016; Zubeldia et al., 2018). Extending this functionality to include constitutive models applicable to other geomaterials would provide unprecedented detail to the simulation of channel evolution by

attrition and quarrying, which are essential erosion processes in fluvial landscapes (Whipple et al., 2000; Lamb and Fonstad, 2010).

CHAPTER 2

BEDROCK CHANNEL EVOLUTION

Introduction

In drainage basins shaped by tectonism and climate-driven surficial erosion processes, the incision and material transport provided by bedrock channels is essential to landscape form. The action of bedrock channels is traditionally couched in terms of an erosion rate, which is usually calculated in numerical models of landscape evolution using the stream power erosion law (Howard, 1994; Whipple and Tucker, 1999) in which hydraulics are related to erosion by local bed shear stress (τ) . By assuming an effective detachment threshold τ_c the erosion rate $\dot{\epsilon}$ can be expressed as:

$$\dot{\epsilon} = K(\tau - \tau_c)^{\gamma} \qquad 2.1$$

where K is an erodibility constant related to lithology and climate and γ is the shear stress exponent (Howard and Kerby, 1983), which effectively serves as tuning parameter to adjust for the proportionality of bedload to suspended sediment load (Istanbulluoglu et al., 2003). Another common variation of involves the approximation of shear stress by the channel slope and discharge, which is approximated by the drainage area to produce:

$$\dot{\epsilon} = KA^{m}S^{n} \qquad 2.2$$

where A is the drainage area, S is the channel slope, and both m and n are positive exponents related to a landscape's dominant erosional mechanism (Croissant and Braun, 2014).

While there have been myriad modeling investigations which use the stream power law to simulate the evolution of a landscape with bedrock channels in ways which are faithful both to

field observations and to the scientific community's understanding of bedrock channel processes, there are drawbacks to using empirical relations to model bedrock channel evolution. In the values of K, m, and n are not measurable in the field and effectively serve as tuning parameters to correct for errors resulting from the approximation of fluvial stresses by slope and drainage area. While the values of constants K, m, and n can be partially constrained by comparing landscape evolution models to field measurements of landforms that have changed over a known amount of time, the values of those constants are both scale-dependent and difficult to apply across domains.

The physical meaning of the constants in the stream power law is difficult to interpret as the constants represent the collective influence of both the physical characteristics and the processes acting on a landscape, which obscures the physics of how and why a bedrock channel evolves over the course of its erosional event history. The dependence of the empirically-derived constants in the stream power law connote that the material response of the landscape depends on the context of the dominant local erosional mechanisms. This connotation is inherently unphysical, as earth materials respond to the forces exerted on them regardless of the source of the forces. Nevertheless, this approach allows for geomorphic response to depend on spatially-variant strength fields to produce numerical landscapes which agree with observations of natural landscapes. Consequently, the stream power law approach successfully simulates a host of earth processes involved in drainage basin morphology from fluvial sediment transport (Carretier et al., 2016) to erosion during orogenesis (Roy et al., 2016) and allows for hypothesis testing in mesoscale earth systems.

In recognition of the importance of strength distributions on earth processes and resultant landscape form (e.g., Roy et al., 2015), Koons and Upton (in prep.) developed the Failure Earth

Response Model (FERM), which unifies the geomorphic treatment of earth materials in a single physics-based framework. The focus of this chapter is the connection of SPH solutions for channelized flow with landscapes produced within the FERM framework.

Methods

The Failure Earth Response Model (FERM)

Whereas τ was previously used to refer to local bed shear stress in and elsewhere, it will now be used to refer to differential stress, which is equal to the difference between the maximum and minimum principal stresses such that $\tau = \sigma_1 - \sigma_3$.

Central to the FERM framework is the idea that all stresses acting on a landscape can be represented by their contribution to a single stress tensor at every point in the domain, and any geomaterial will fail when local differential stress strength (τ) exceeds the local strength (C) of that material. Stress-strain analysis is used to determine if an arbitrary volume of earth material is in failure, which occurs when $C{:}\,\tau < 1$. This treatment separates the mechanical properties of earth materials and the stresses acting on them from environmental context and shifts time-dependency from the geomaterial to the characteristic frequency and magnitude of stressors, thereby eliminating the need for an erodibility term.

The FERM approach does not mandate any single failure criterion or stress-strain analysis solver, but the present formulation is implemented in the Itasca FLAC3D solver (Itasca, 2017) and uses a version of the Mohr-Coulomb failure criterion with modified Griffith theory formulation to accommodate reversible tensile plastic strains. As such, all geomaterials within the FERM domain are prescribed strength parameters cohesion, tensile strength, and friction angle. FLAC3D is also able to generate fracture network geometries with power-law spatial distribution, and all material zones along the fracture planes may be prescribed strength

parameters which are separate from the surrounding bedrock. This allows for simple prescription of heterogeneous strength fields in spatial configurations which are self-similar and therefore valid across spatial frequencies.

The most recent formulation of the FERM erosion process is written in Python using the Itasca Python module which is used to interface with FLAC3D. The Python code is available in Appendix A: , but the basic functionality provided by the code is as follows:

- Identify all sections ("zones") of earth material at the surface of the model
- For each zone, determine if the material is in failure
- If the zone is in failure and is transportable by hillslope or fluvial processes, remove the zone
- Add newly-exposed zones to the list of surface zones

The models shown in Figure 2.1, Figure 2.2, Figure 2.3, and Figure 2.4 share the following properties:

- Bulk Modulus = $1*10^{14}$ Pa
- Shear Modulus = $2*10^{13}$ Pa
- Density = 2700 kg/m^3
- Cohesion = $9*10^5$ Pa
- Tensile Strength = $9 * 10^4$ Pa
- Friction angle = 30°

- Discrete fracture network with Fisher orientation and power law positional distribution
- Fracture zone cohesion = $9e^4$ Pa
- Fracture zone tensile strength = $9e^3$ Pa
- Fracture zone friction angle = 10°

Results

The role of channelized flows in the removal of weak material and subsequent exposure of underlying strong material is explored in Figure 2.3, Figure 2.4, and Figure 2.5. Both Figure 2.1 and Figure 2.2 show the initial conditions of the model, which is first prescribed a bedrock fabric with heterogeneous rock strength and subsequently topped with a layer of weak unconsolidated material. The scenario shown in Figure 2.4 uses forces calculated with SPH simulation of flow through the channel to determine where fluvial stresses are present. The presence of any non-zero fluvial stresses in the direction of mean flow satisfies a transport condition for zones which are in failure. Figure 2.5 shows that hillslope processes and fluvial erosion removes ~44% more material by volume than hillslope processes alone.

Figure 2.1 – Strength:Stress Before Erosion

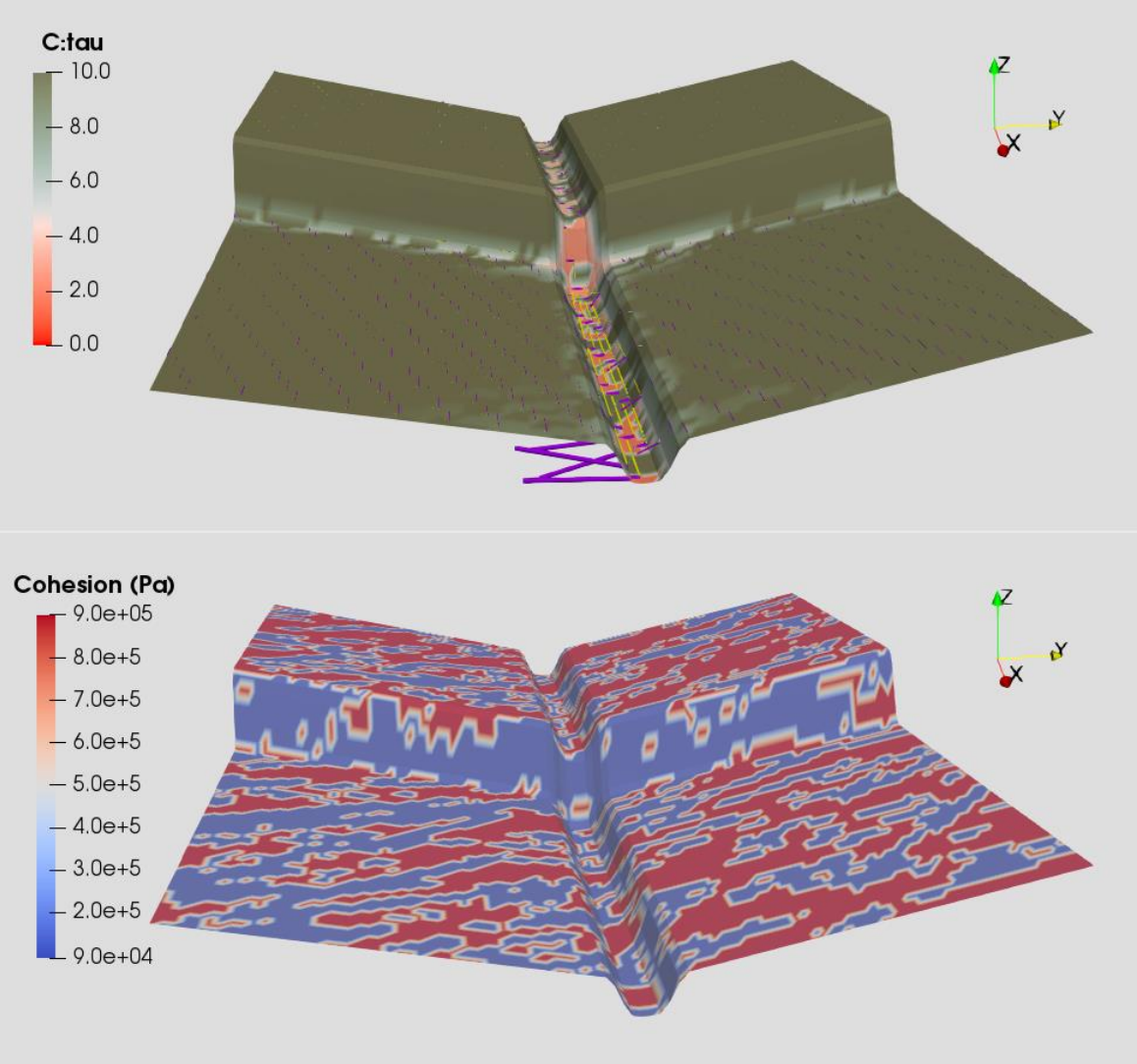

The top and bottom frames show $c:\tau$ and cohesion, respectively, prior to erosion, and prior to conversion of the top layers of the domain to unconsolidated material (Figure 2.2). Principal stresses are shown by colored glyphs, where σ_1 is purple, σ_2 is green, and σ_3 is yellow. Note that the heterogeneous strength field shown in the bottom frame produces a low $c:\tau$ (approaching failure) in the channel, but the low-cohesion material on the hillslope has a high $c:\tau$ (stable, not close to failure). This suggests that the hillslope-generated stresses and the relatively high angle of the channel walls are primary drivers of failure within the bedrock channel.

Figure 2.2 – Strength:Stress Before Erosion, with Unconsolidated Material Atop

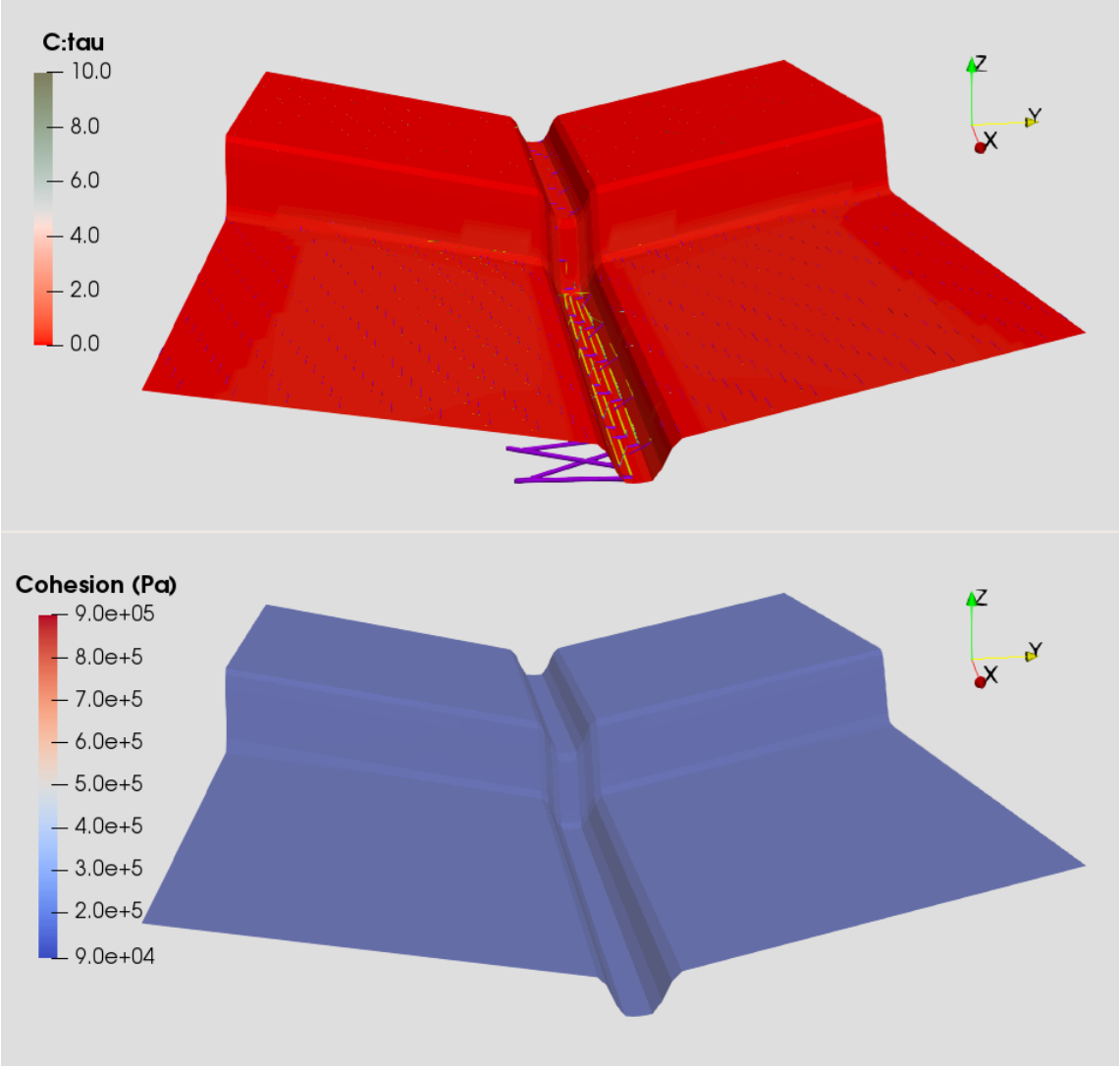

Once the top two layers of the model domain are given strength properties characteristic of unconsolidated material (cohesion = $1*10^3$ Pa, tensile strength = $1*10^2$ Pa, friction angle = 5°), all material at the surface is in failure ($c:\tau < 1$). This is the initial condition which gives rise to the results presented in Figure 2.3 and Figure 2.4.

Figure 2.3 – Strength:Stress After Erosion, Without SPH Fluvial Stresses

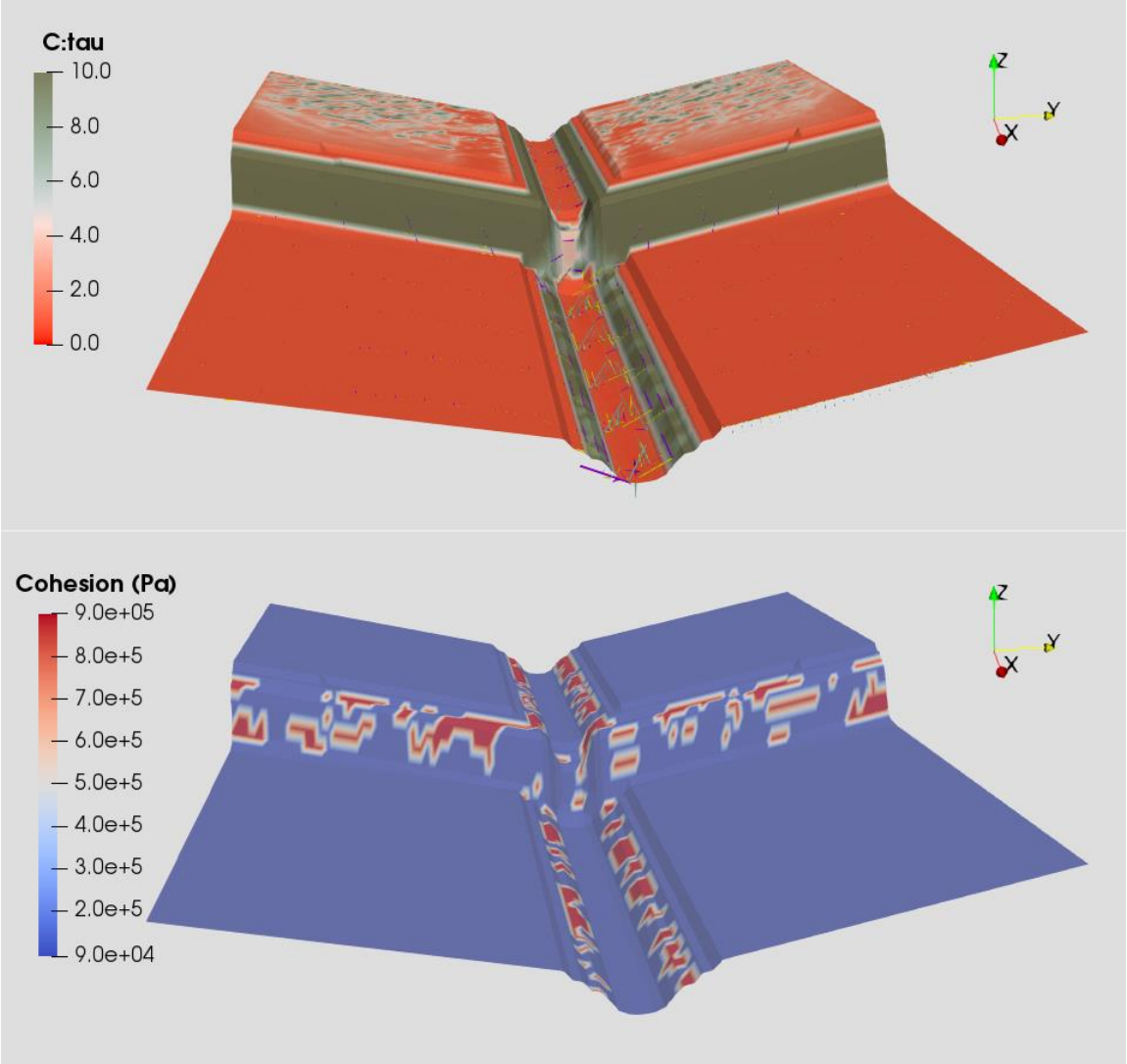

Unconsolidated material in failure which was removable by hillslope processes has been removed from the domain, but the rest of the material in failure remains in situ as there is no transport mechanism (no fluvial stresses) to remove it.

Figure 2.4 – Strength:Stress After Erosion, With SPH Fluvial Stresses

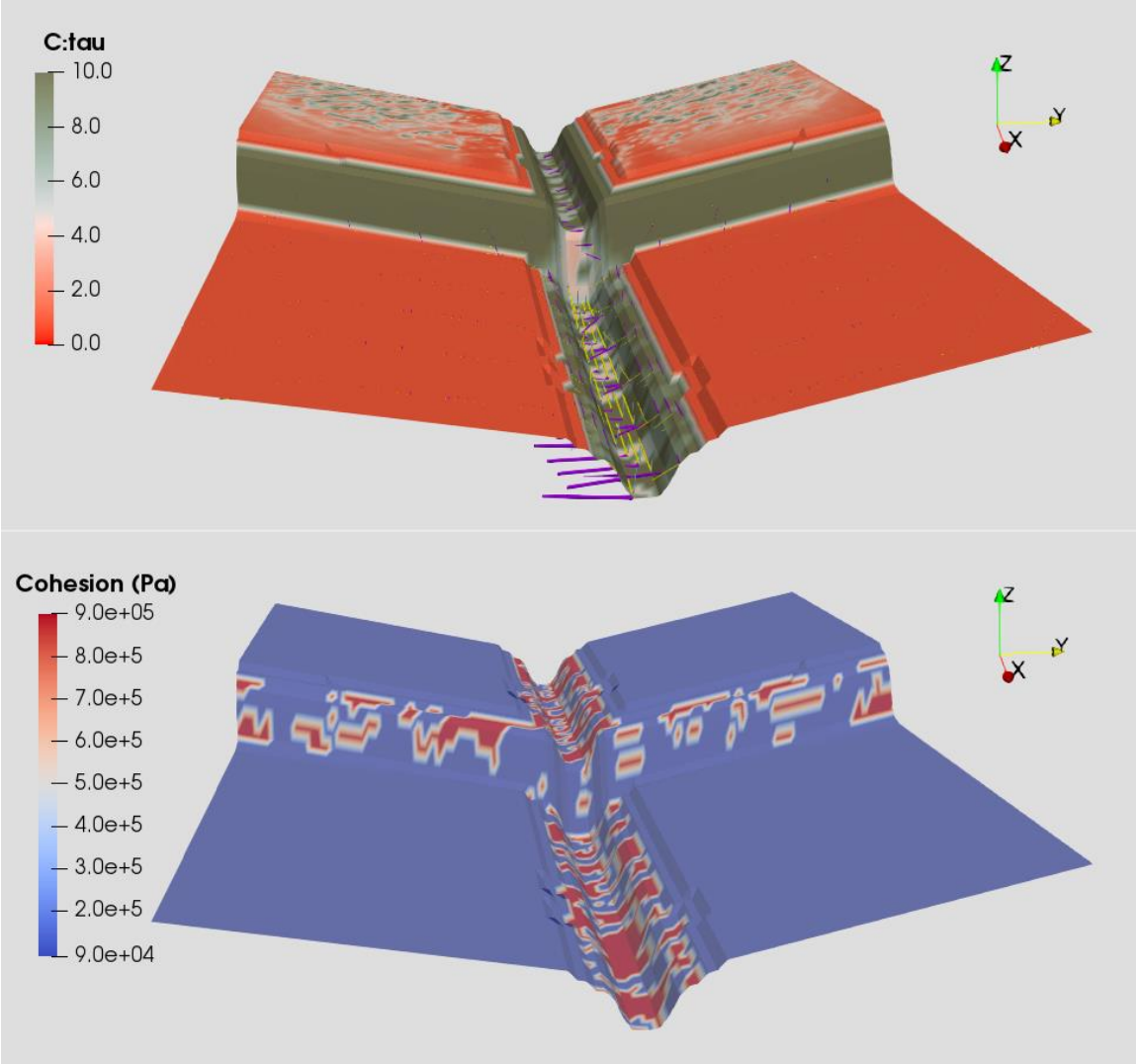

Unconsolidated material in failure has been removed by hillslope processes and fluvial transport. Weak material in failure remains in situ, but the channel has exposed the stronger rock which lay below the upper layers of unconsolidated material. Note that the strongest rock is far from failure ($c: \tau \geq 10$) and the rock which intersects the fracture zones is stable, but far less so than the stronger surrounding bedrock.

Figure 2.5 – Total Erosion and Erosion Rates, With and Without Fluvial Transport

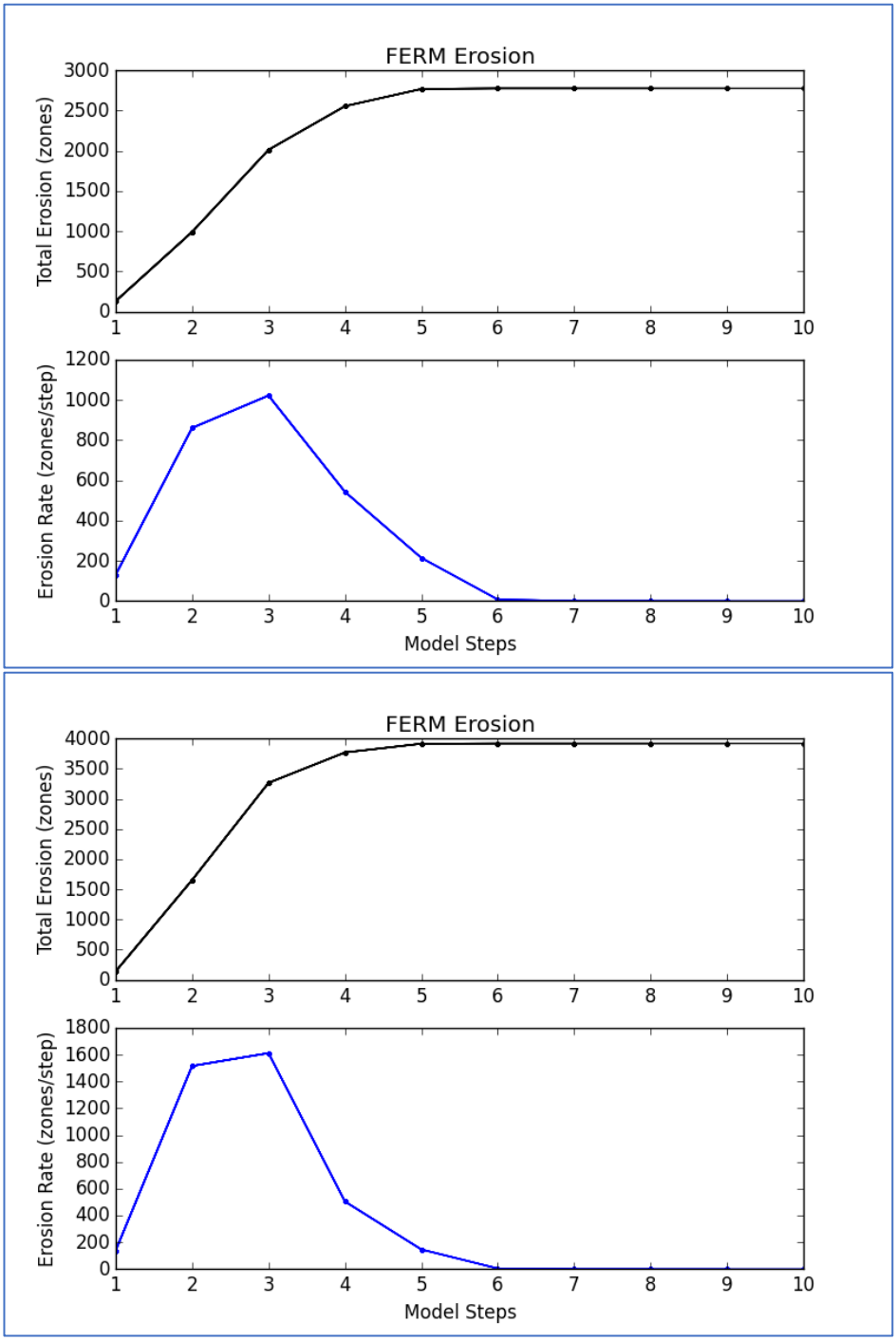

The top frame shows the erosion associated with the dry channel without fluvial stresses (Figure 2.3), and the bottom frame shows the erosion associated with the channelized flow case (Figure 2.4). With fluvial erosion, ~44% more material by volume is removed than by hillslope processes alone.

Connecting SPH Flows to a Finite Element Earth

Coupling SPH solutions to FERM connects the kinematics of water flowing over landscapes with the forces produced by hydraulic action. Figure 2.6 shows the iterative coupling process between DualSPHysics and FERM. Adding hydraulic forces calculated via SPH maintains a clear connection between the governing physics of fluid dynamics and the estimated contribution of hydraulic forces to the local stress tensor. Hydraulic forces are passed to FERM once the SPH flow approaches a steady state. As the landscape changes in FERM, the evolving landscape geometry is passed back to DualSPHysics to calculate the new flows and associated forces. Throughout the iterative process of coupling FERM and DualSPHysics outputs, the hydraulic forces depend on and change with the landscape and may vary in strength and direction over sub-meter scales, as they do in nature.

Figure 2.6 – Coupling FERM with DualSPHysics

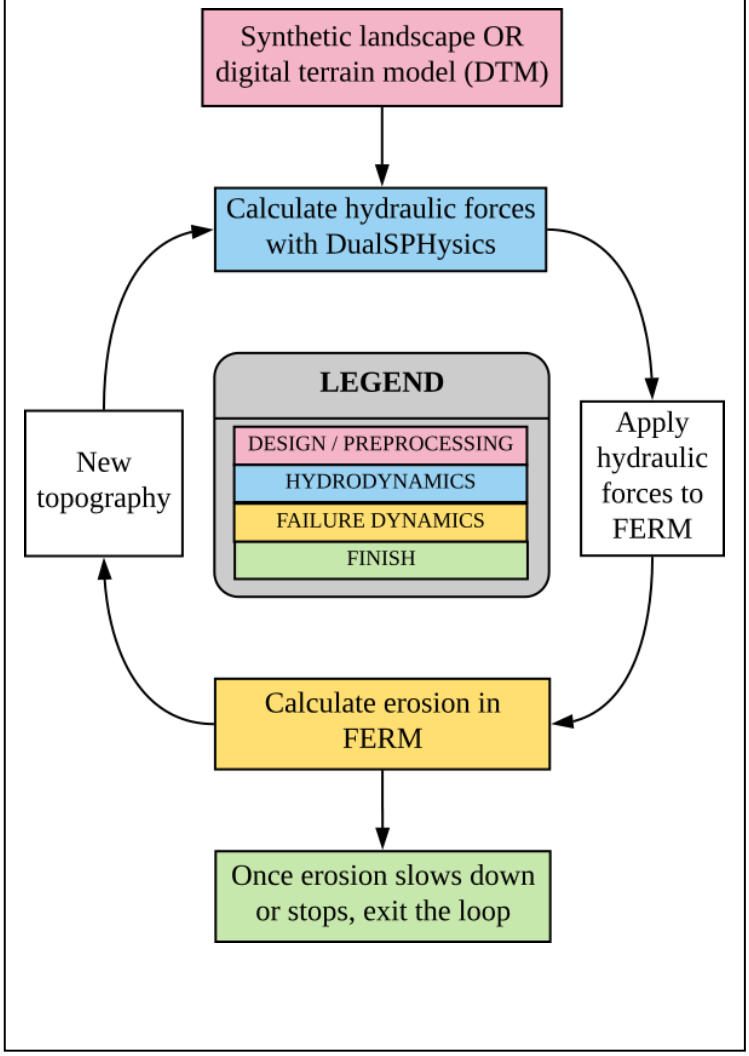

Figure 2.7 – Strength:Stress After Erosion, With SPH Fluvial Stresses

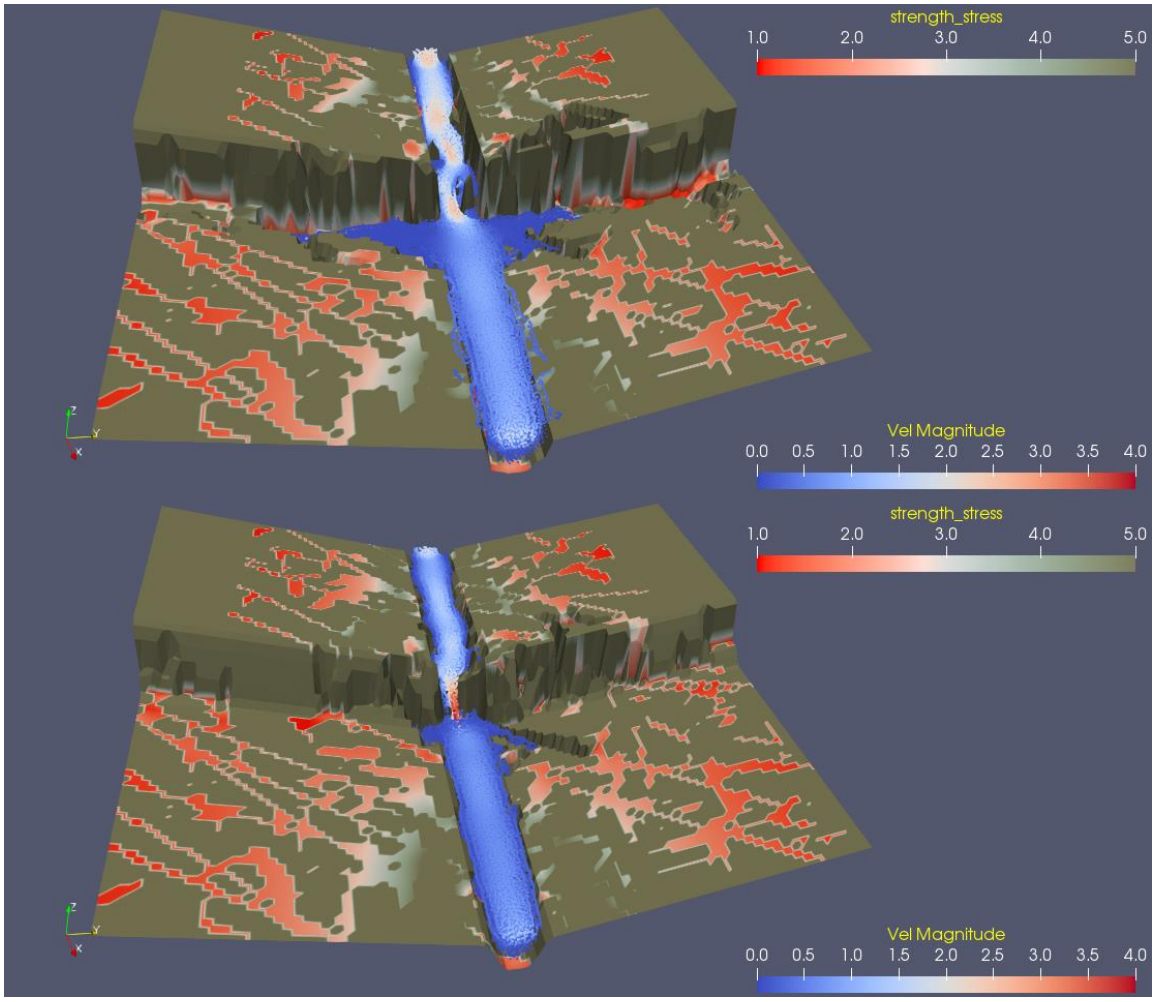

Both frames show SPH flows through FERM landscapes generated after 20 cycles of SPH-FERM coupling as described by Figure 2.6. The bedrock in the top frame has cohesion and tensile strength values ($5*10^4$ Pa and $5*10^3$ Pa, respectively) which are an order of magnitude higher than the bedrock in the bottom frame. Each landscape has weak zones defined by a fracture network. The weak zones have a cohesion which is two orders of magnitude less than the upper frame scenario and one order of magnitude less than the lower frame scenario. Even though the bottom frame scenario has weaker bedrock, the strength gradient is lower, and there is markedly less erosion than the stronger bedrock scenario shown in the top frame, in which strength gradients are an order of magnitude higher.

Figure 2.8 – Hydraulic Forces Before and After Coupled SPH-FERM Erosion

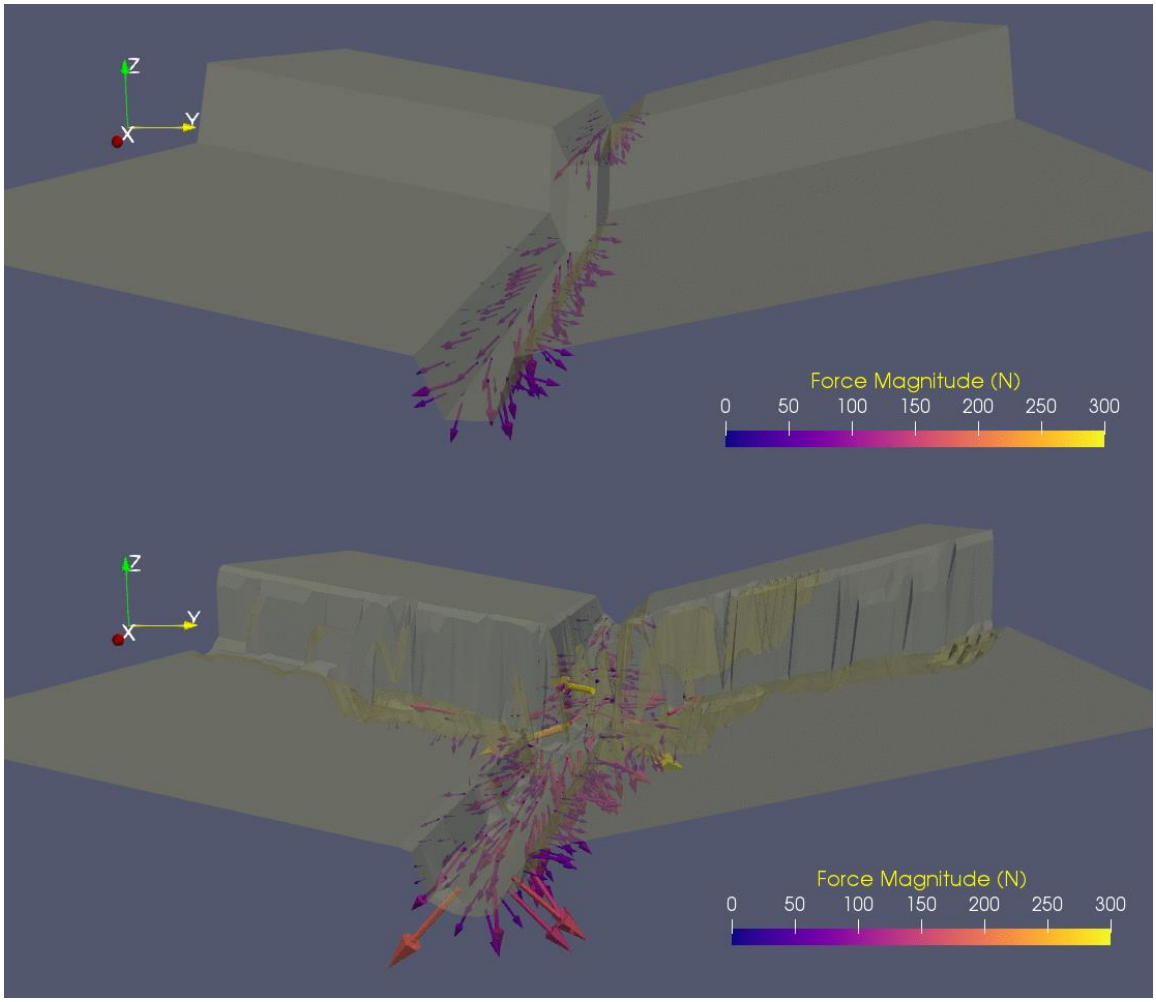

The top frame shows the pre-erosion state of a channel with bedrock characterized by $5*10^4$ Pa cohesion, $5*10^3$ Pa tensile strength, and a 30° friction angle, with weak zones intersecting fracture planes which have cohesion and tensile strength values an order of magnitude less than the surrounding bedrock and a 20° friction angle. The force vectors in the bottom frame show the increased magnitude and directional complexity of flows through the eroded landscape.

Discussion

The landscapes presented in this chapter use a physics-based approach to quantify failure in a variety of local rock fabric strength and stress conditions. Like many landscape change models, the present implementation of FERM is detachment-limited, which implies that so long as stresses exceed a detachment threshold, material is presumed to be removable by transport mechanisms (fluvial, hillslope, glacial, etc.). Shobe et al., (2016) demonstrate that detachment-limited assumptions can lead to inaccurate erosion modeling when transport forces are not sufficient to remove material away downslope or downstream. By introducing an SPH-derived fluvial stress contribution to FERM, there is a now way to justify removal of failed material within a channel (Figure 2.4) and to justify failed material remaining in situ wherever transport forces are absent (Figure 2.3). The importance of accounting for material transport is illustrated in Figure 2.5, which shows that hillslope processes and fluvial erosion removes ~44% more material by volume than hillslope processes alone.

While the present implementation of fluvial stresses in FERM is a positive development, the fluvial transport conditions do not yet represent a first principles approach. To provide a more robust mechanism for determining the post-failure motions of geomaterials in contact with flowing water, the failed material should be included in the SPH solution to determine whether or not the material is removed from the domain by entrainment or hillslope processes. The DVI method presented in CHAPTER 1 could be a robust way to model the motions of failed material as it falls away from hillslopes or is swept away by flows, and it would organically determine whether there are sufficient transport forces to initiate movement of the failed material. If failed material isn't removed from the domain, it may provide a buttressing effect which could provide stability to the surrounding landscape, thereby limiting further erosion.

An important finding is revealed by the erosion patterns shown in Figure 2.7, in which two rock fabrics differing in cohesion and tensile strength have weak rock in fracture zones which has the same strength values in both scenarios. Consequently, the strength gradients are much higher in the top frame than the bottom frame. Even though the top frame has stronger rock fabric, there is more erosion and greater hydraulic complexity as the flow follows the zones of weakness. In the bottom frame, which has less strong rock fabric but lower strength gradients, there is less erosion and the flow is routed in a more direct path since it doesn't have to divert around strong rock fabric. This phenomenon speaks to the critical importance of strength heterogeneity in determining the patterns and total erosion in fluvial landscapes, as supported by Roy et al. (2015).

The Failure Earth Response Model represents a fundamentally different approach to modeling landscape change. The 3D physics-based treatment of earth fabric provides detailed information about the stability of the landscape throughout the entire model domain while maintaining strong links between material properties, landscape processes, and landscape form. The modular approach to landscape stressors from deep Earth to surficial processes allows modeling of very simple to highly complex landscapes. The challenge of connecting stress-strength analysis to the temporal domain is somewhat addressed by connecting time-dependent SPH flows with FERM. Accounting for changing hydrodynamics over the course of days, weeks, years, and 10^x years remains challenging. One possible solution is to use SPH to inform less computationally-expensive means of approximating hydraulic stresses over long timescales. A compelling avenue of further development on this front is training a machine learning model to recognize patterns in hydraulic stresses at various discharges acting on a variety of geometries. This would allow high

degrees of temporal flexibility with arbitrary definition of extreme discharge or drought event frequency and duration.

Since FERM uses geomaterial strength parameters which are measurable or easily referenced in geotechnical engineering literature, it makes sense to compare and validate FERM models with field measurements in natural settings. FERM is uniquely positioned to model complex landscapes with many coexistent or competing stressors which produce stress gradients with high spatial frequency, which is often the case in tectonically-active regions associated with earthquakes, landslides, and other geohazards. As such, establishing benchmark models of varying complexity which are validated with field experiments will help to assess FERM's performance with modeling Earth processes which are intrinsically difficult or dangerous to observe and measure.

CHAPTER 3

3D FLOW SIMULATION TO INFORM RIVER REHABILITATION DECISION-MAKING EFFORTS

Abstract

Following the 2013 removal of the Veazie Dam in the lower Penobscot River, the reemergence of remnant logging structures ("boom islands") in the former dam impoundment raises questions about what should be done, if anything, with the derelict structures. Knowledge about the impacts of the boom islands on federally-protected diadromous fish species can help to inform decision-making efforts about dam removal projects involving remnant infrastructure. Detailed knowledge of the water flow velocity conditions around boom islands is central to assessing the impact of logging industry infrastructure on fish habitat, but there are challenges associated with direct measurements and traditional numerical approaches to predicting their hydraulic effects. I apply 3D hydraulic modeling calibrated with 3D hydraulic velocity measurements collected by an Acoustic Doppler Current Profiler (ADCP) to address ecological questions that require a detailed knowledge of the hydraulic conditions of the Penobscot River. With these detailed measurements and modeling results, I partially resolve the influence of relict logging structures on the hydraulic conditions which impact aquatic habitat for federally-protected diadromous fishes.

Introduction

In-stream structures alter aquatic habitat by adding flow complexity throughout the water column, which in turn can lead to changes in substrate and bed morphology (Abbe and Montgomery, 1996). Flow kinematics around in-stream structures are well-studied, largely owing to the civil engineering community's interest in understanding vortex-induced scour,

especially in the case of flow around bridge piers (e.g., Arneson et al., 2012). Even so, few studies provide detailed information about the 3D kinematics of flow past in-stream structures, and the problem domain is often reduced to one or two dimensions. In terms of aquatic habitat, knowledge of the velocity in the z-dimension is relevant to assessing habitat suitability for creatures which require certain velocity conditions for spawning, rearing, and feeding. In Maine's Penobscot River, structures called "Boom Islands" or "Boom Piers" were built to facilitate the routing of logs down the river (Figure 3.1). Although some of these structures were submerged following dam construction in the early 20th century, recent dam removals have led to their exposure above the water surface. The influence of the newly-exposed boom islands on the velocity structure of the Penobscot River could have implications for habitat suitability for diadromous fishes in the river ecosystem. By quantifying the influence of boom islands on the velocity structure of the Penobscot River, we can add to the body of knowledge that goes into the decision-making process about river restoration and rehabilitation efforts.

The Penobscot River has a 22,000 km^2 drainage area and delivers a mean annual discharge of 340 m^3/s to its outlet at Penobscot Bay (Hooke et al., 2017). After passing through mountainous western Maine, the lowland area leading to Penobscot Bay flows over glacial sediments with some areas of exposed sandstones and limestones of the Vassalboro Formation. The course of the Penobscot's main stem and major tributaries, which connect the woods of northern and western Maine to the ocean, was desirable to the logging industry in the 19th and early-to-mid 20th centuries. After logs were cut, they were delivered to downstream mills for processing. With the logging activity on the Penobscot came logging infrastructure, and though much of this has been dismantled or destroyed by natural processes, some of it remains in the river more than a century after construction.

One of the major components of the Penobscot River Restoration Project (PRRP) was the removal of the Great Works and Veazie dams (Opperman et al., 2011). The primary motivation to remove the dams was to restore access of the Penobscot River to eleven species of diadromous fishes that use the Penobscot as spawning grounds. Veazie Dam was the most seaward barrier to diadromous fish migration, situated at the approximate upstream extent of tidal influence of the river at 47 river kilometers (rkm), or 47 kilometers upstream of the mouth of the river at Penobscot Bay. The 2013 removal of the Veazie Dam decreased local water surface elevation and increased the water surface slope. As the water surface lowered, previously-submerged logging infrastructure became exposed (Figure 3.2 and Figure 3.3).

There has been interest in evaluating to what extent the hydraulic response to the removal of the Great Works and Veazie dams has impacted habitat suitability for various diadromous fishes in the Penobscot River (e.g., Haro et al., 2015; Johnston, 2016). By constructing a habitat suitability index (HSI) for the various at-risk fish species, researchers determine which regions of the Penobscot River are challenging for fish migration or spawning. In addition to substrate texture and channel depth, channel velocity is a major determinant of habitat suitability. Johnston (2016) created habitat suitability maps for shortnose sturgeon (Acipenser brevirostrum) in the Veazie Impoundment Area, which spans rkm 47 to rkm 52. The maps depict habitat suitability under five characteristic spring discharge conditions. Modeled velocities that contributed to the HSI estimates were calculated with River2D, a 2D depth-averaged finite element hydrodynamic model which solves for mass conservation and conservation of the horizontal components of the momentum equation. While 2D depth-averaged models are useful for capturing the kinematics of flows with hydrostatic pressure distributions and near-uniform vertical velocity distributions, they are not designed to simulate the vertical velocity distribution of a water column or resolve

the three-dimensional (3D) effects associated with complex flows that may occur around structures (Steffler and Blackburn, 2002). HEC-RAS is an example of a 1D hydraulic model which solves for the 1D energy equation, applying solutions to the 1D Shallow Water equations where flow is rapidly-varied, such as past in-stream structures (US Army Corps of Engineers, 2016). While computationally inexpensive, HEC-RAS has difficulty resolving complex flows around structures, with numerical instabilities arising from rapid lateral contraction and expansion of the channel.

Orthoimagery shown in Figure 3.3 reveals that lower section of the Veazie Impoundment area (approximately 47-48.5 rkm) has at least 30 exposed boom islands after the Veazie Dam was removed. Maps produced by Johnston show that this same area contains regions of low-to-moderate habitat suitability. Since in-stream structures have been shown to promote aquatic habitat (e.g., Boavida et al., 2011; Roni et al., 2015) taking the influence of the boom islands into consideration may impact the HSI for Atlantic sturgeon and other at-risk fish species. The main goal of this investigation is to quantify the effects of boom islands on channel velocities and determine the spatial perturbance of flow caused by these structures, using the Penobscot River as a case study. To address these topics, we must turn to methods capable of resolving channel velocity structure in three dimensions.

Figure 3.1 – Boom Islands in Maine Rivers

"Boom Piers" or "Boom Islands" are rectangular structures constructed with wood (often hemlock) and rock. Interconnecting the structures with booms, which are long logs connected by chains, created transportation lanes in the river to properly route logs to different mills downstream and allowed logs to be sequestered as necessary. [A] shows the 1893 construction of a boom island on the Androscoggin River, courtesy of Greater Rumford Area Historical Society (www.mainememory.net). [B] shows log booms connecting two boom islands, courtesy of The Patten Lumbermen's Museum.

Figure 3.2 – Images of the Veazie Dam Removal: Before, During, and After

Landsat satellite imagery and USDA orthoimagery visualized in Google Earth show the Penobscot River's response to various stages of the Veazie Dam removal, which began on July 22, 2013. With the dam in place in the November 2011 panel, the water upstream of the dam is high enough to submerge relict logging structures. The August 2013 panel shows a sediment plume moving downstream of the dam site during the dam removal process. The May 2015 panel shows that following the dam removal, the water surface height is low enough to reveal relict logging structures.

Figure 3.3 – Orthoimagery of the Penobscot River (~53 rkm) Before and After the 2013 Veazie Dam Removal

USDA orthoimagery of the Penobscot River (approximately rkm 47-48) visualized in Google Earth shows the Penobscot River's water surface elevation response to the 2013 removal of the Veazie Dam. With the dam in place in the October 2011 panel, the water upstream of the dam is high enough to submerge relict logging structures. The May 2015 panel shows that following the dam removal, the water surface height is low enough to reveal clusters of previously-submerged boom islands.

Methods

Acoustic Doppler Velocimetry

3D velocity measurements of the Veazie Impoundment area of the Penobscot River were collected with an Acoustic Doppler Current Profiler (ADCP) on June 4, 2018. The ADCP unit, a RDI 1200 kHz Workhorse, was configured to use a bin size of 0.25 m and an initial bin depth of 0.61 m below the water surface, with a sampling rate of 90 ms per ping, 1 ping per ensemble, and an average ensemble interval of 1.12 s. The initial post-processing phase involved interpolation of the raw data onto a uniform grid, removal of the bottom 10% of data due to side slope effect error, removal of data ensembles with signal return of less than 85% high-fidelity data, exclusion of velocities in excess of 5% of the maximal flow, and a correction for ship speed and direction as per Joyce (1989). We chose a reference coordinate for each section of measurement to calculate the distance to each water column measurement along a lengthwise axis. Each section of measurement consisted of north-south and east-west velocity components aligned to a distance-depth plane.

Velocity measurements were collected around three boom islands around rkm 49 and a transect around rkm 48 across the full width of the channel. Measurements of flow conditions around each of the three structures were divided into upstream, downstream, river right, and river left sections. Boom island “CR1” (44.8440°, -68.6975°, WGS84 datum) was determined to be most representative of a typical boom island in terms of geometry, proximity to other structures, distance from the riverbank, and orientation with respect to the dominant channel flow direction. CR1 also produced more usable data than the other two survey locations.

Because the initial bin depth was 0.61 below the water surface and the ADCP measurements do not extend to the channel bed, the low water surface elevation on the day of the survey limited

the number of bins collected for each profile such that no data was returned for between ~50-75% of the water column. Secondary post-processing to fill in data gaps consisted of extrapolation down to the channel bed and up to the water surface (Figure 3.4). Velocity extrapolation with the assumption of a logarithmic velocity profile is an established method of filling in gaps in field observations of channels (Wilcock, 1996).

One of the challenges with collecting velocity measurements in a channel is estimating an expected discharge value to compare with measured discharge to verify velocity data integrity Johnston (2016) used a regression technique based on delineations of local watershed boundaries to estimate the additional water discharge contribution from the drainage area downstream of the West Enfield gage station, the nearest upstream discharge measurement location in the Penobscot River mainstem. A discharge estimate for the Veazie Impoundment area is calculated by adding the estimated discharge contribution to the measured West Enfield gage station value. Another way to estimate the Veazie Impoundment discharge is by relating the measured discharge and drainage area of the nearby Kenduskeag Stream and applying the relation to the drainage area of the Veazie Impoundment area. The Kenduskeag Stream provides a relevant comparison to the Veazie Impoundment area of the Penobscot because unlike the West Enfield portion of the river, the Penobscot's flow isn't well-regulated at the Veazie Impoundment area, which is approximately 14 rkm downstream of the nearest dam (Milford Dam). These two approaches to discharge estimation are referred to as the "West Enfield Method" and the "Kenduskeag Method" in Table 3.2 in the results section.

Figure 3.4 – Velocity Measurements Across the Veazie Impoundment Area

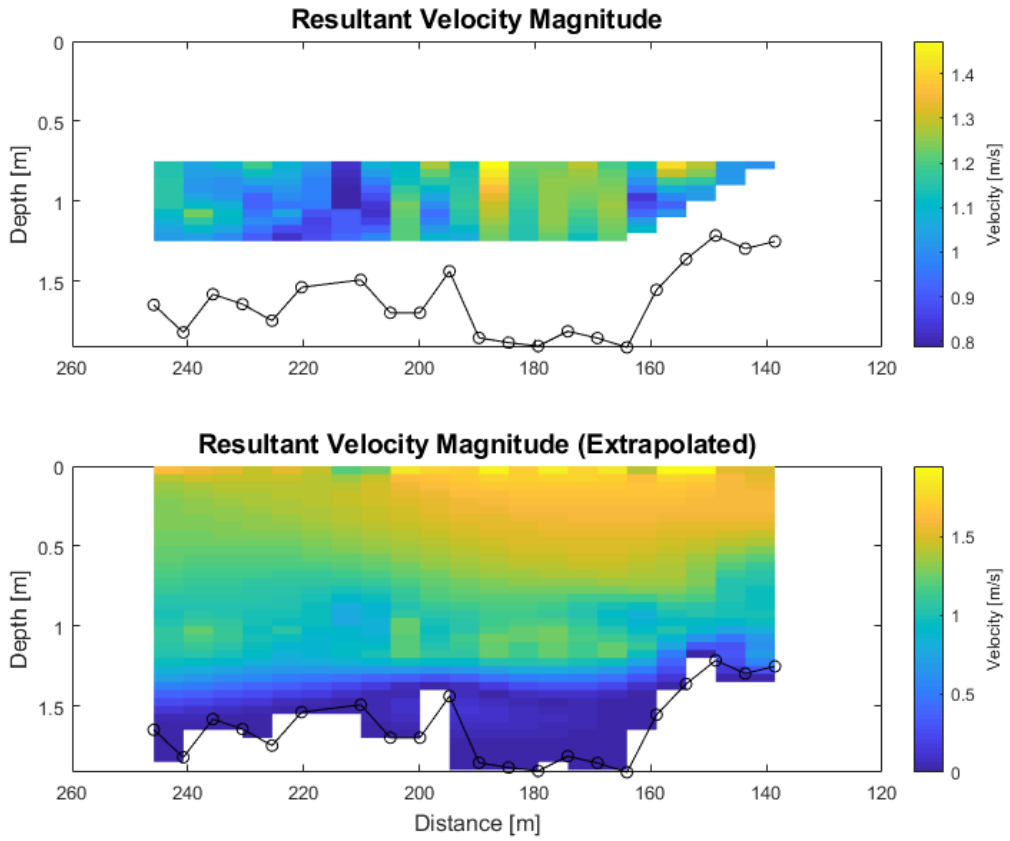

The top frame shows the region of data collection for a full transect across the width of the Penobscot River, shown here from an upstream-facing perspective. The black line represents the channel bottom and the top of the y-axis represents the water surface. The gaps between the collected data region, the channel bottom, and the water surface were filled by extrapolation. After estimating the surface velocity and near-bed velocity using a logarithmic fit in keeping with the "law of the wall" principle (von Kármán, 1930), extrapolation was performed using a Laplacian least-squares fit (D'Errico, 2012). In this transect, 26.5% of the profile was captured by ADCP measurements, requiring extrapolation for the remaining 73.5% of the profile.

Smoothed Particle Hydrodynamics

I used the 3D velocity measurements collected with an ADCP unit to constrain and validate 3D computational fluid dynamics solutions calculated using Smoothed Particle Hydrodynamics (SPH) to capture the 3D effects of a boom island on the velocity structure of the Penobscot River. While detailed 3D velocity measurements are possible with Acoustic Doppler

Velocimetry, collecting measurements over large swathes of river reaches is impractical. Numerical modeling of fluid dynamics in a channel is a practical means of overcoming the scaling issues associated with direct measurements and is made even more practical by using a SPH solver capable of leveraging high-performance computing resources.

The formulation and general description of Smoothed Particle Hydrodynamics (SPH) and description of the DualSPHysics solver is given in the Methods section of Chapter 1. DualSPHysics v4.3 Beta was used to perform the hydraulic modeling presented in the Results section on page 50. There are many advantages to choosing DualSPHysics, most notably the optimization of the code for GPU parallel processing. Running the DualSPHysics code on a GPU vastly decreases solution times, thereby allowing high-resolution and/or large-domain cases to be executed efficiently. DualSPHysics v4.3 Beta is the first release of the code to introduce inlet-outlet boundary conditions. This allows explicit definition of the velocity profile of particles entering or exiting channelized flows.

I derived the vertical velocity profile prescribed to the simulation of flow around a boom island from the horizontally-averaged velocity of the upstream portion of the ADCP measurements at boom island CR1. Important SPH parameters chosen for this model include the use of a Wendland kernel, artificial viscosity scheme ($\alpha = 0.05$), Symplectic time-stepping algorithm, and an inter-particle distance of 20 cm. The model is run for one minute of simulation time to allow for settling of initializing perturbations as the flow approaches a steady state. The model domain is 100 m long in the flow-wise direction, 60 m wide, with an imposed inlet and outlet surface elevation of 2.2 m. The boom island in the SPH model has the same dimensions and orientation with respect to the dominant flow field as boom island CR1. The Dynamic Boundary Condition described in Chapter 1 was used to impose a no-slip condition between the boundary

particles which make up the synthetic boom island and the surrounding fluid. In the absence of detailed bathymetric measurements, a flat channel bottom was used and prescribed the same Dynamic Boundary Condition treatment as the synthetic boom island.

Statistical Comparison of Measurements and Numerical Results

Comparing ADCP measurements and SPH numerical results requires simplification of the velocity structure. Because the zone of data collection by the ADCP is relatively small compared to the total flow field, and because it is intrinsically difficult to compare flow velocities on continuous grids when the grid coordinates do not form a straight line (Figure 3.5A), I compared the vertically-averaged velocities of ADCP measurements and SPH results to assess model fitness. Statistical measures of data variability and model fitness, such as variance, the sum of squares error, and the root mean squared error, are used to compare the measured and simulated vertically-averaged velocities.

Results

ADCP Measurements

The velocity measurements from the full transect across the width of the Veazie Impoundment area was used to estimate the discharge on the day of the survey. As shown in Figure 3.4, there are gaps in the raw measurements which complicate the process of estimating discharge. By extrapolating the ADCP data for the unmeasured portions of the water column and by assuming that the unmeasured lateral boundaries of the data collection track account for 15% of the flow (Figure C3.), I arrived at an adjusted discharge measurement which is close to the expected discharge for this area (Table 3.2).

Table 3.1: Reference Gage Discharge Measurements

USGS Gage Number	Channel	Location	Discharge on June 4, 2018, 08:00 (m^3/s)	Estimated Discharge at Veazie Impoundment (m^3/s)
01034500	Penobscot River	West Enfield, Maine	178.4	211
01037000	Kenduskeag Stream	Bangor, Maine	20.2	188

The estimated discharge for the Veazie Impoundment area is calculated using two different techniques based on the discharge values of nearby reference gages. Although the estimate based on the West Enfield gage is on the Penobscot River, the Kenduskeag Stream may provide a better approximation of discharge for the Veazie Impoundment area of the Penobscot because its flow is similarly unregulated.

Table 3.2: ADCP Discharge Measurements

Vertical Extrapolation	Account for 15% discharge loss at the lateral margin	Discharge (m^3/s)	Percent of Expected Discharge, (West Enfield method)	Percent of Expected Discharge, (Kenduskeag method)
No	No	42.7	20.2	22.7
No	Yes	49.1	23.3	26.1
Yes	No	145.5	69.0	77.4
Yes	Yes	167.3	79.3	89.0

While the measured discharge doesn't match up well with the discharge estimate made with the West Enfield method described in the Methods section (page 43), it does come within 11% of the estimate made with the Kenduskeag method. The low discharge measurements may be a product of an inaccurate estimation of discharge loss at the lateral margin, an extrapolation error, instrumental uncertainty, or a combination thereof.

Figure 3.5 – ADCP Transect Map for Boom Island CR1

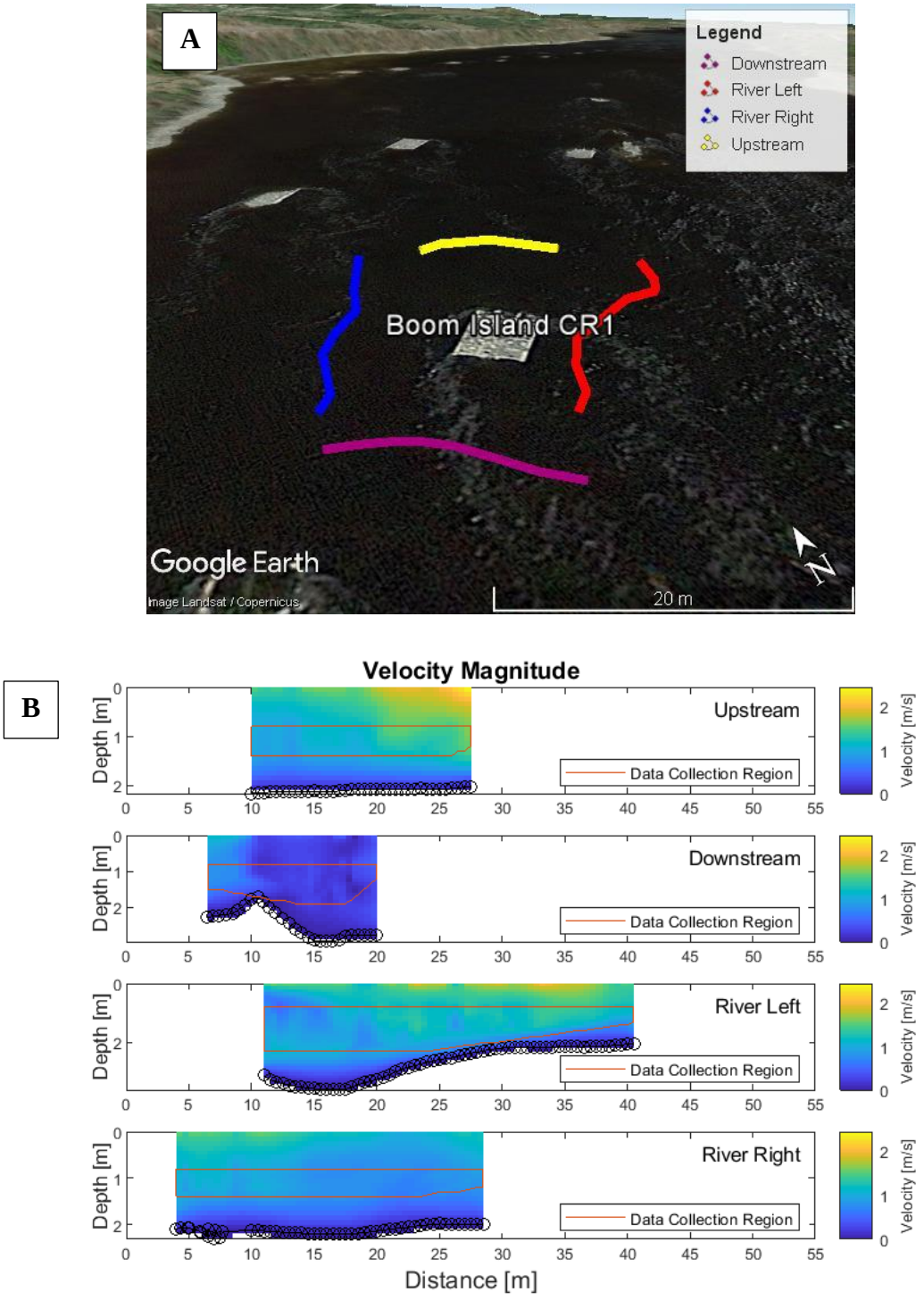

[A] shows the ADCP transect map. After performing five passes around boom island CR1 with the ADCP unit, the straightest transects with the most complete velocity profiles were selected for the upstream, downstream, river left, and river right sections. [B] shows the two-dimensional (X-Y) velocity measured by the ADCP and extrapolated outside the data collection region bounded by the red line. Reported distances are distances from a reference coordinate chosen for each section.

Figure 3.6 – Vertically-Averaged Velocity Derived from ADCP Measurements

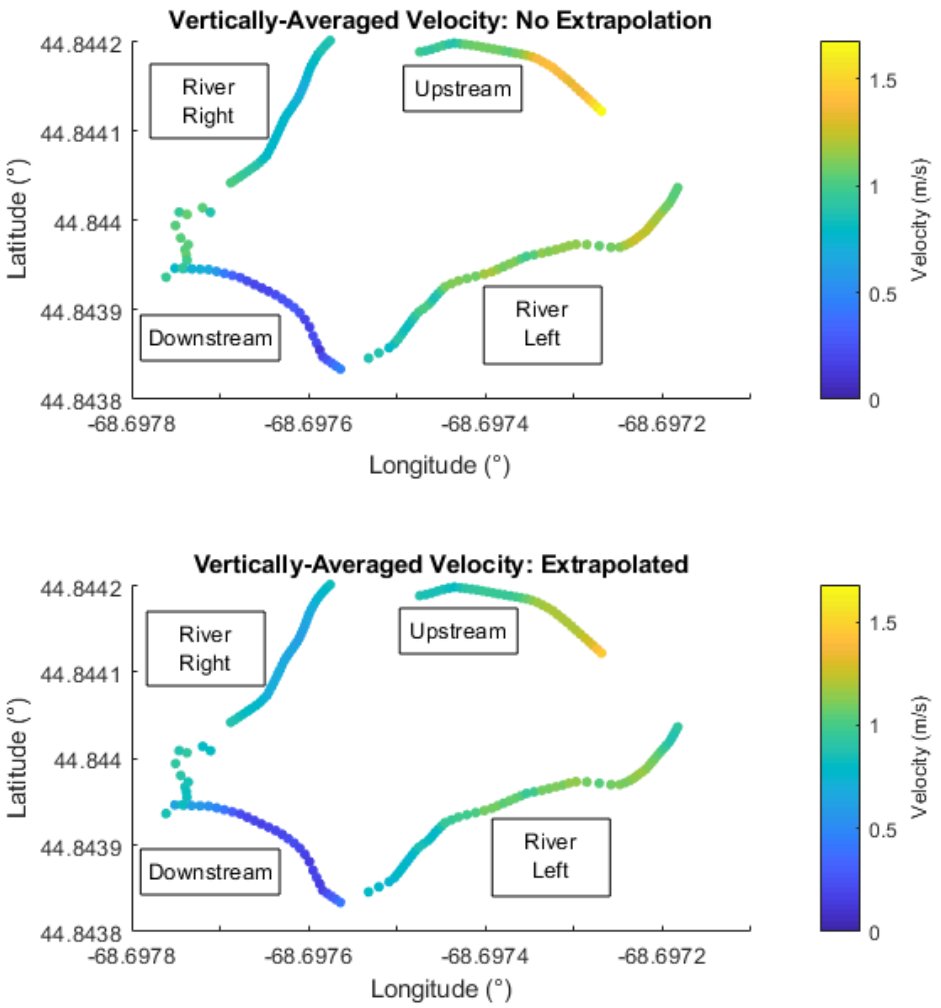

The vertically-averaged velocity from the raw measurements and extrapolated 2D profiles show that the vertical velocity profile of the raw measurements is well-translated to the extrapolated velocity profile. The largest discrepancy between raw and extrapolated data is in the river-left side of the upstream section, in which the extrapolated velocity somewhat under-estimates the vertically-averaged velocity of the raw measurements. In addition to extrapolation error, this could also be a product of the average depth of the zone of measurement, which at 0.478 times the water surface height above the channel bed, may be slightly shallower than the mean column velocity depth. Since the extrapolated velocity adequately represents the velocity measurements and extends throughout the entire water column, the vertically-averaged extrapolated velocity was chosen for comparison to the SPH model results.

SPH Simulation of Flow Around a Boom Island

The horizontally-averaged velocity profile from the upstream section of the ADCP measurements was used to explicitly define the inlet velocity profile of the SPH simulation. The sampling locations for vertically-averaged velocity are presented in Figure 3.7. As shown in Figure 3.8, an eddy forms behind the boom island as the flow approaches a steady state, which is also seen in the satellite imagery of boom island CR1 shown in Figure 3.5A.

Figure 3.7 – Transect Schematic for SPH Boom Island Simulation

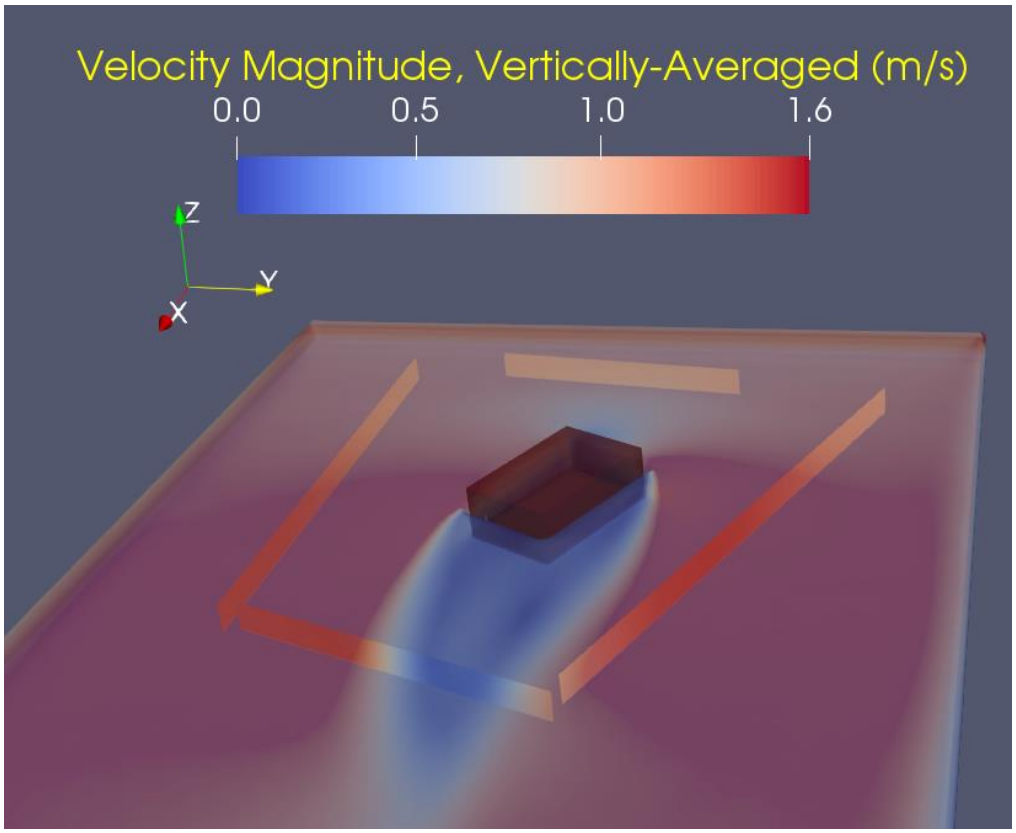

The vertically-averaged velocity of the SPH was calculated after placing numerical velocity probes at regular, closely-spaced intervals throughout the fluid domain. The vertically-averaged velocity was interpolated into a 3D volume by Delaunay triangulation, then slices of the interpolated velocity domain were positioned to resemble the ADCP data collection paths shown in Figure 3.5A. The resulting profiles are compared to ADCP vertically-averaged velocity in Figure 3.6.

Figure 3.8 – Flow Past a Boom Island: SPH Velocity with Vectors

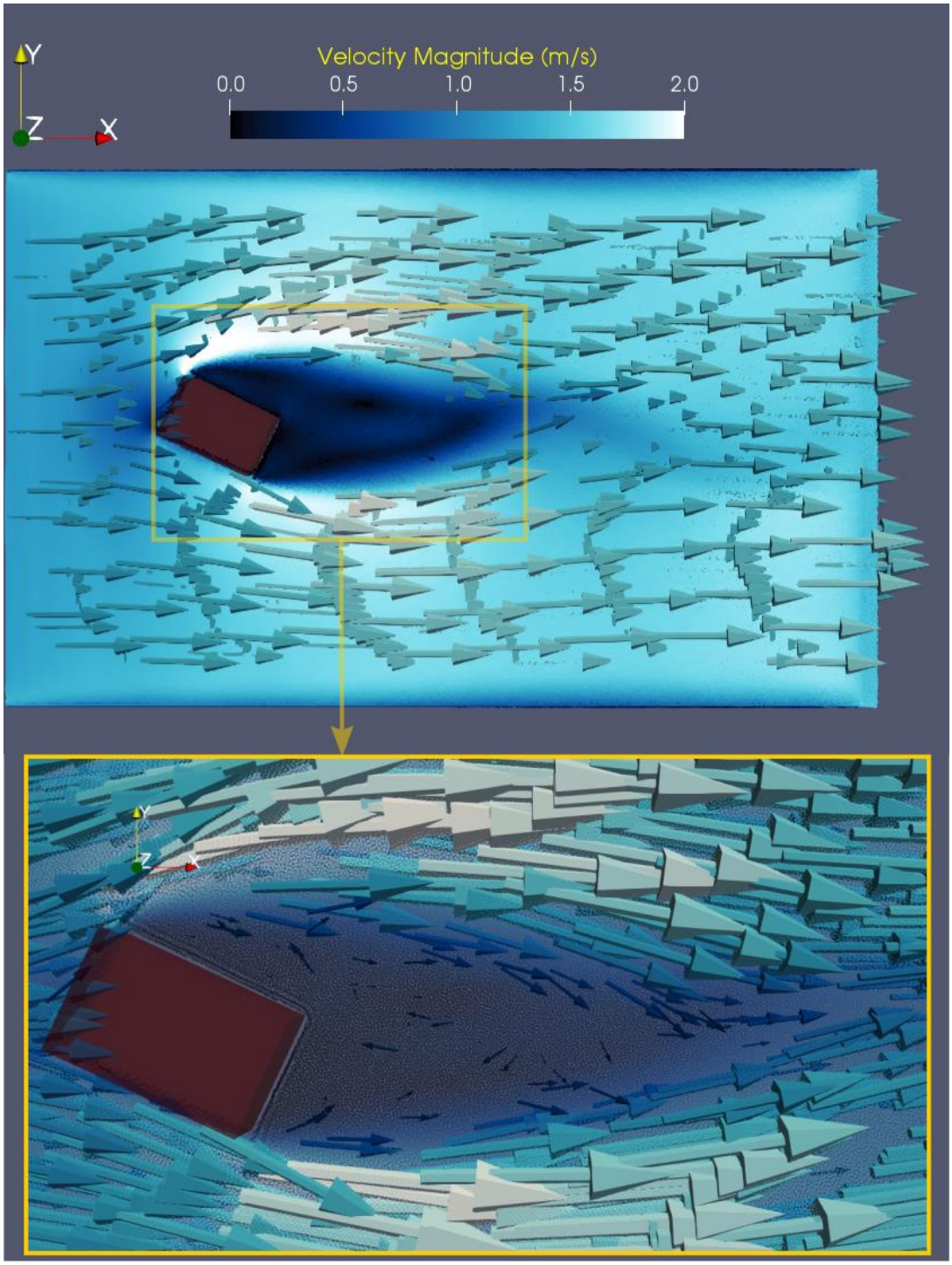

As the flow approaches a steady state, the flow deflects around the boom island and creates a point of stagnation immediately downstream. A close view of the velocity vectors shows that there is slight flow reversal in the eddy that forms behind the boom island.

Figure 3.9 – Vertically-Averaged Velocity Modeled with SPH

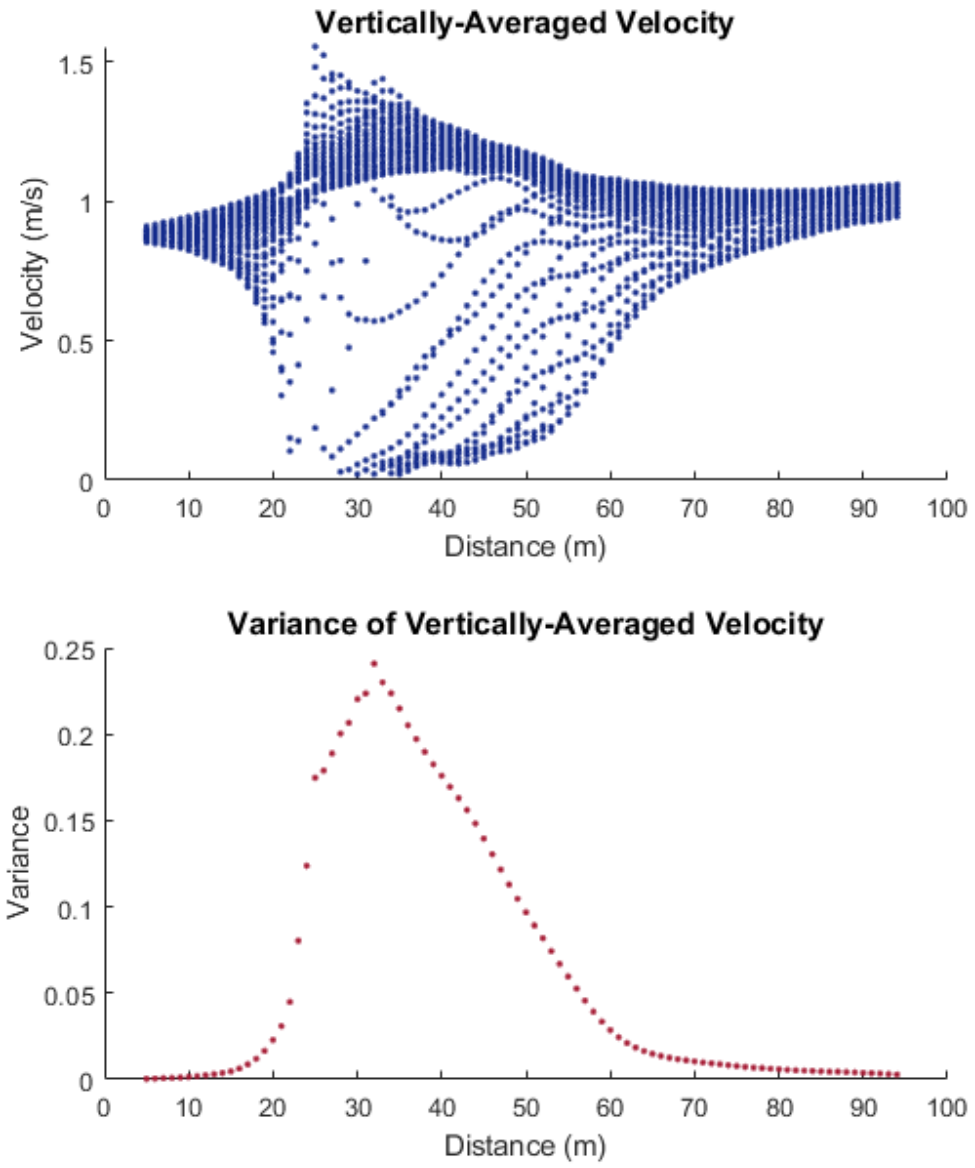

The perturbation to the velocity field created by the boom island decays with distance, and the reorganization of flow makes the effect of the boom island negligible near the 80 m mark, roughly 45 meters downstream of the boom island. The boom island extends from 23 m to nearly 34.5 m in the x-direction and displays mild influence on the upstream velocity and a profound influence on the downstream velocity that begins to decay near the 60 m mark, just upstream of the tip of the wake created by the boom island. The wake zone is marked by the low-velocity strands between the 30 m and 70 m marks.

Figure 3.10 – Relation of SPH Velocity to Shortnose Sturgeon Habitat Suitability

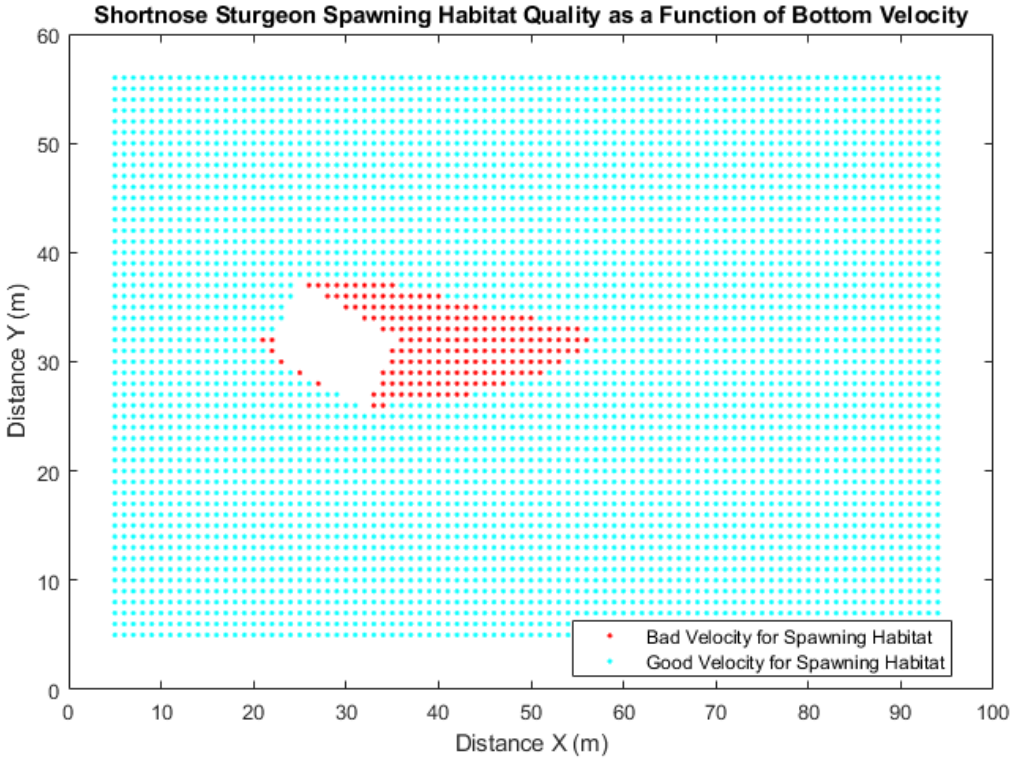

The red points indicate a region in which the modeled velocity magnitude between the channel bed and 0.39 m above falls outside of the threshold values for velocity conditions that promote shortnose sturgeon habitat suitability (velocity between 0.36 m/s and 1.2 m/s) as defined by Johnston (2016). In this case, all red points fall below the minimum velocity threshold. Note that the velocity inlet condition is based on measurements taken when the flow was approximately half of the 115-year median value of flow for the same day, June 4. This flow is also about half of the lowest discharge value (5^{th} percentile) considered by Johnston for the March – May spring discharge period.

Comparison of Measurements and Model Results

Figure 3.11 – Vertical Velocity Profile: Upstream Section

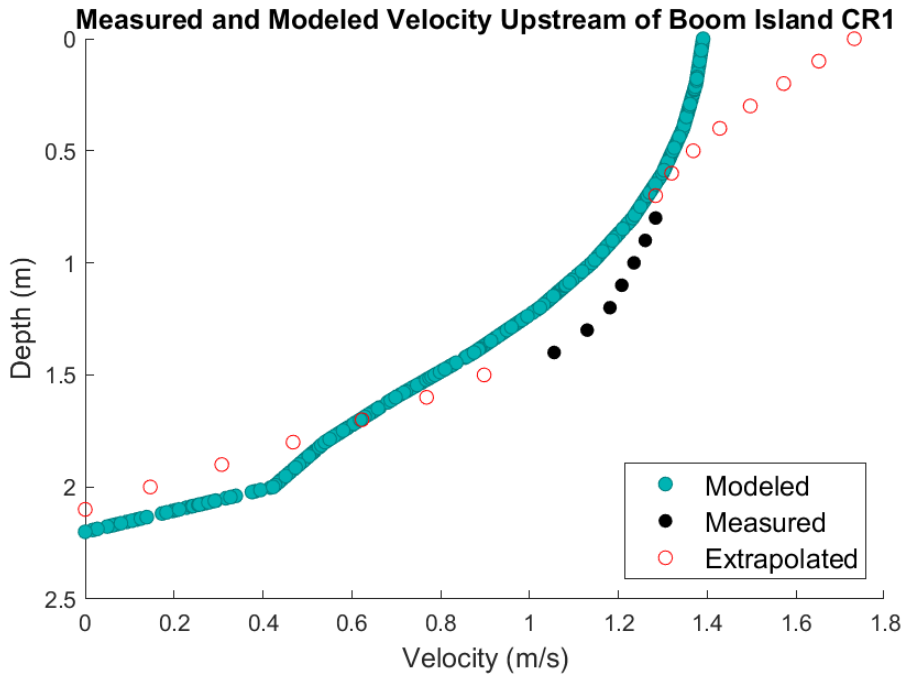

Figure 3.12 – Vertical Velocity Profile: River Right Section

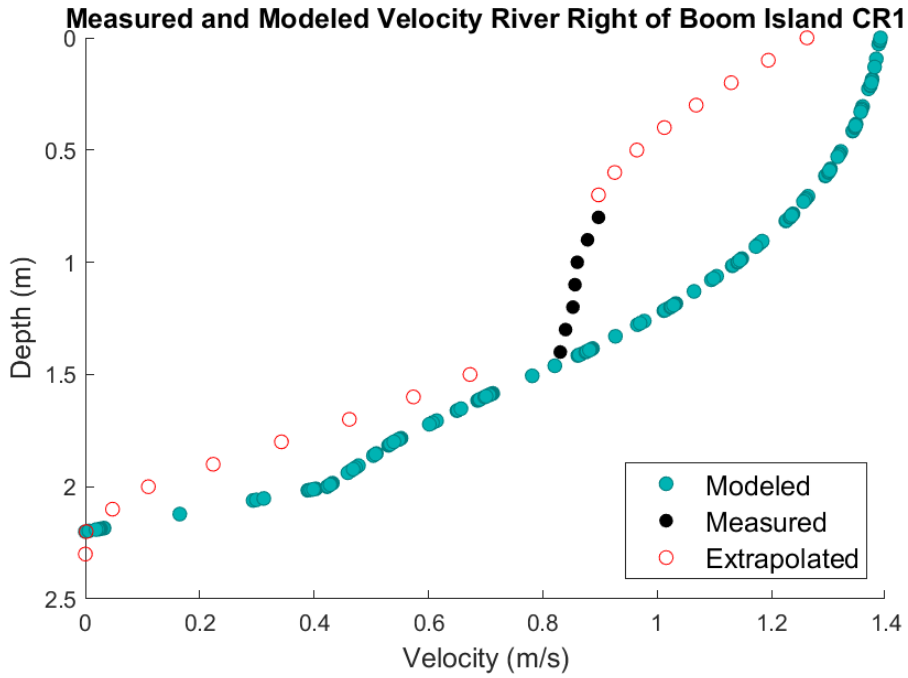

Figure 3.13 – Vertical Velocity Profile: Downstream Section

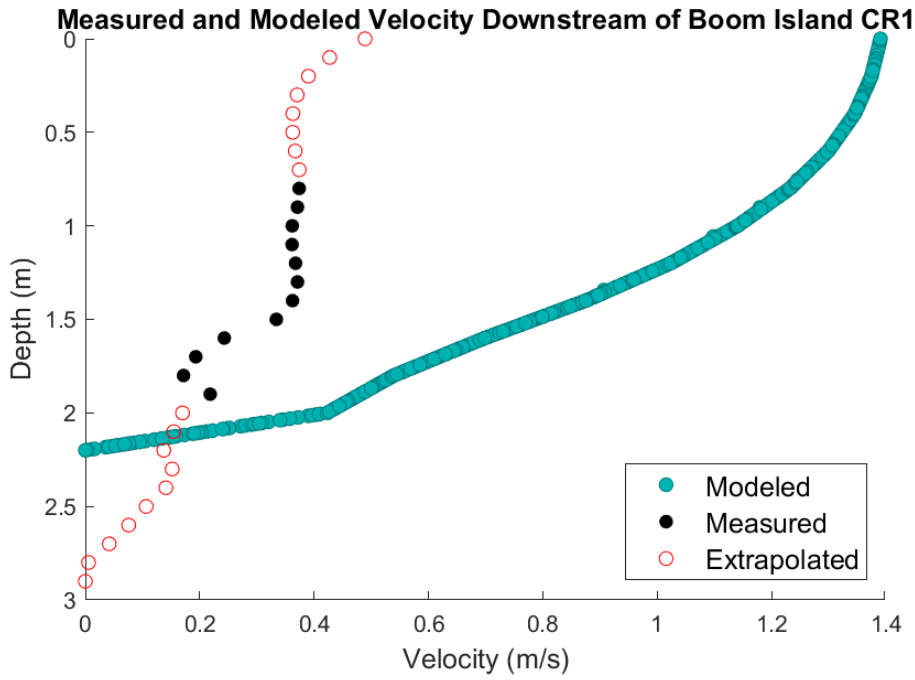

Figure 3.14 – Vertical Velocity Profile: River Left Section

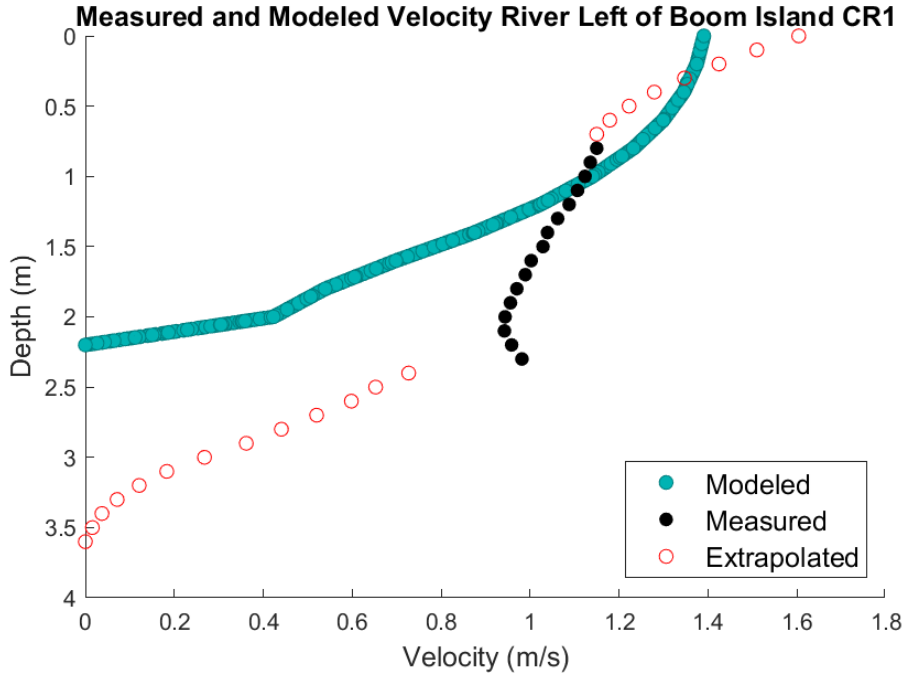

Figure 3.15 – Fitness of Modeled Results and Measurements: Upstream Section

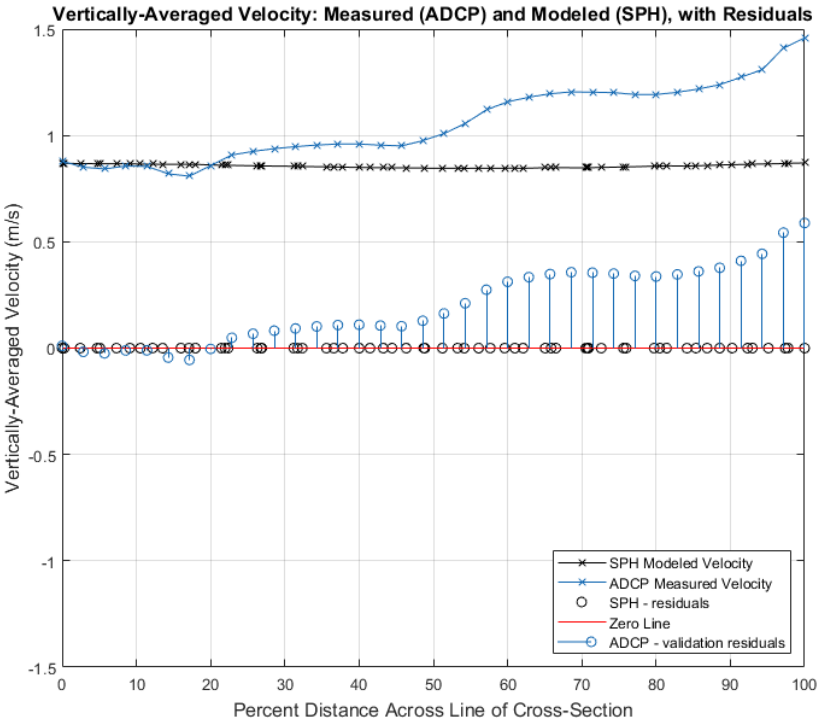

Figure 3.16 – Fitness of Modeled Results and Measurements: River Right Section

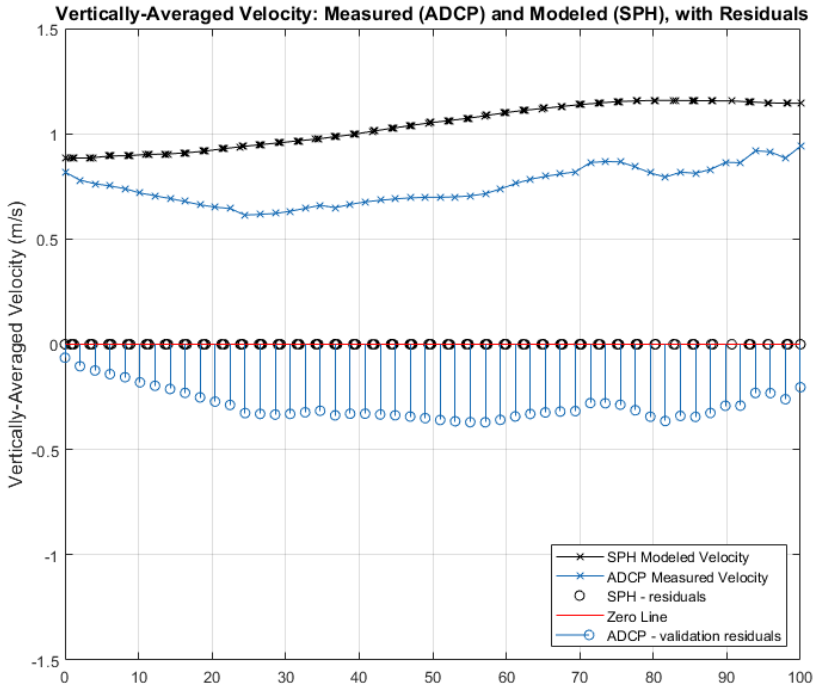

Figure 3.17 – Fitness of Modeled Results and Measurements: Downstream Section

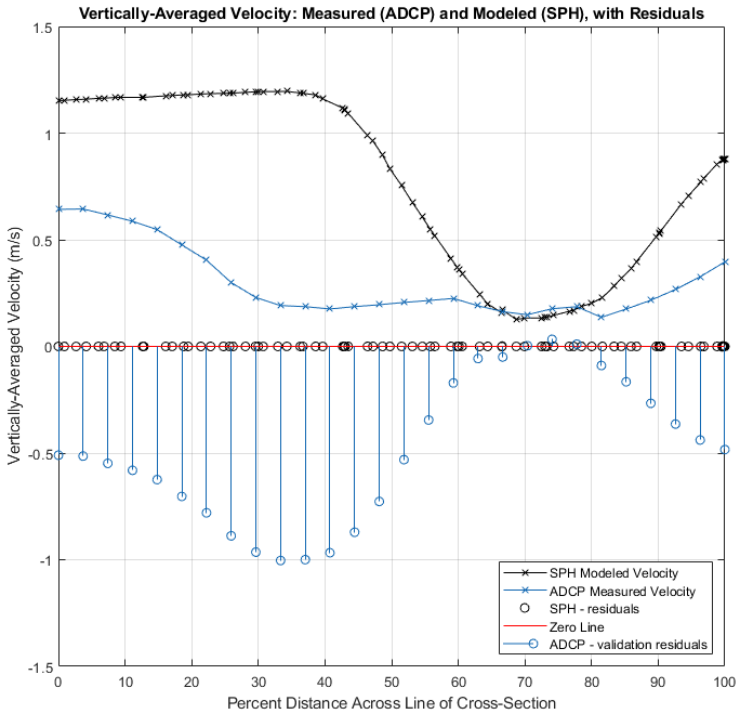

Figure 3.18 – Fitness of Modeled Results and Measurements: River Left Section

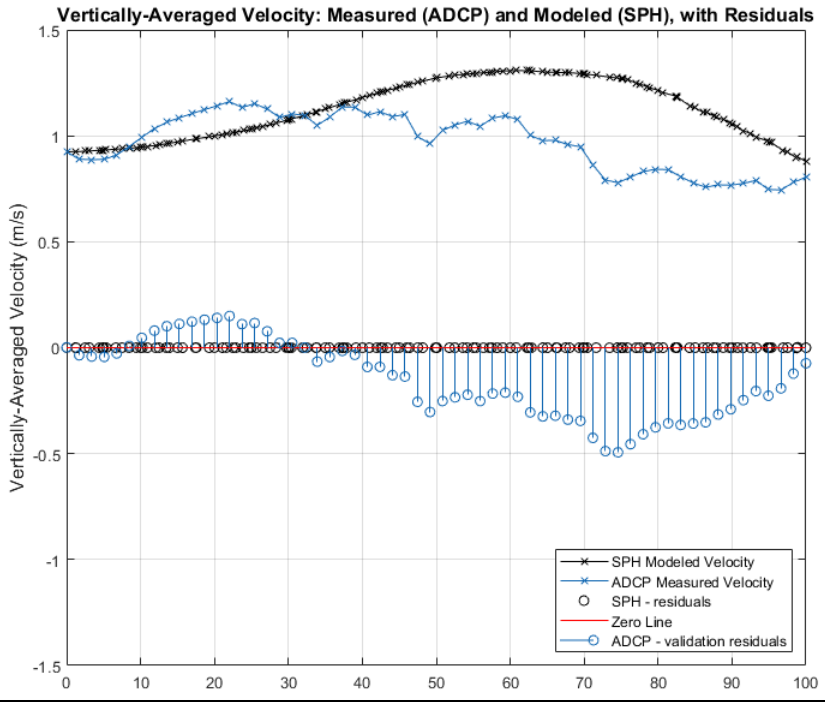

Table 3.3: Statistical Comparison of Measured and Simulated River Velocity

Section	SSE	RMSE	ADCP Variance	SPH Variance
Upstream	2.581	0.268	0.0318	0.0001
Downstream	9.708	0.589	0.0185	0.0198
River Left	3.365	0.237	0.0279	0.1649
River Right	4.427	0.298	0.0080	0.0105

The Sum of Squares Error (SSE) and Root Mean Squared Error (RMSE) measure the fitness of the modeled vertically-averaged velocity (SPH) and the vertically-averaged velocity measurements (ADCP). The variance measures the spread of the velocity data.

Discussion

ADCP velocity measurements shown in Figure 3.6 and Figure 3.7 and corresponding discharge measurements reported in Table 3.2 provide a baseline for comparison with SPH model results. Before comparing the fitness of the model results to the measurements, it is important to consider the uncertainty associated with the ADCP measurements. Figure 3.5B shows the data collection region inside of the water column that accounts for 25-50% of the total water column, the rest of which must be extrapolated down to the channel bottom and up to the water surface. Assuming a no-slip boundary condition for the channel bottom helps to constrain the downward extrapolation. Without knowledge of water velocity at the surface (the topmost measurement was 0.71 m below the water surface), the upward extrapolation from the zone of measurement can't be well-constrained and depends strongly on the extrapolation algorithm selection. Plate, Spring Metaphor, Neighbor Average, Laplacian, Laplacian Least Squares, and Biharmonic extrapolation algorithms were tested for water column velocity extrapolation. The Laplacian least-squares fit algorithm was chosen selected because it was the only algorithm which tended towards monotonically increasing velocities from the channel bed through the zone of data collection and up to the surface.

Even with the assumption of 15% discharge loss at the lateral margins of the channel (Figure C3.1), discharge estimates using the two techniques compared in Table 3.1 show that the velocity measurements (with vertical extrapolation) are below the expected discharge value. While there is uncertainty associated with both discharge estimation techniques, the extrapolated discharge is 6.2% higher than the measured discharge at the West Enfield gage, which isn't justifiable considering the additional drainage area associated with the ~52 rkm downstream distance of the Veazie Impoundment area from the West Enfield gage. In the absence of any specific reason to suspect that the ADCP velocity measurements might generally be low, the discrepancy between estimated and measured discharge is likely due to extrapolation error within the vertical column and/or at the lateral boundaries of the data collection area. Still, the extrapolated velocity produces a discharge within 11% of the closest estimate (produced by the "Kenduskeag Method" discussed on Page 43). Considering the uncertainties associated with the necessary extrapolation of 50-75% of the water column coupled with the general agreement of the modeled discharge and the lower discharge estimate, the ADCP velocity measurements should be regarded as reasonable.

The ADCP measurements shown in Figure 3.4, Figure 3.5B, and Figure 3.6 show a velocity structure that is consistent with flow past an oblique bluff body. The wake produced by the deflection of flow by the boom island is evident in the downstream velocity section, which marks a point of stagnation typical of flow around a bluff body. The orientation of the boom island is such that the upstream-facing short side deflects the main channel flow at a much sharper angle than the upstream-facing long side. This is reflected in the velocity profile by a river-left velocity that is higher than the river-right velocity, especially in the upstream portion.

Deviations from simple cases of flow past a bluff body appear in the form of lateral flow variability in the upstream section and variability in each measured section (e.g., Figure 3.4 and Figure 3.5**).** The higher velocity of the channel-left side of the upstream section is likely due to the presence of the wake tail of the nearest upstream boom island (Figure 3.5) combined with increasing proximity to the center of the channel. The variability in each measured section is likely due, at least in part, to changing bathymetry along with a complex channel substrate composed of pebbles and cobbles (Johnston, 2016). Increased velocity with proximity to the channel center and the effects of bathymetry and substrate on the velocity field are examples of natural variability that is very difficult to replicate in a numerical model.

The SPH model shown in Figure 3.7 and Figure 3.8 simplifies the geometry and boundary conditions of the natural system. In the absence of bathymetric data for the simulated region, the SPH model uses a flat channel bottom without any granular substrate. The water surface elevation is uniform across the domain and is calibrated to the upstream section of the ADCP measurements. The velocity inlet condition is prescribed using a vertical profile calculated from the horizontally-averaged profile of the upstream section of ADCP measurements. Without including details of the natural system beyond the boom island dimensions, boom island orientation, water surface elevation, and a velocity inlet condition based on field measurements, the SPH model reproduces a velocity structure similar to the flow around boom island CR1. Flow around the boom island results in a pattern of velocity deflection and wake formation reflected in both the ADCP measurements (Figure 3.6) and, qualitatively, to the satellite imagery shown in Figure 3.5.

Both qualitative and quantitative comparison of the vertically averaged velocities of the ADCP measurements and SPH model are useful for evaluating model fitness. Figure 3.11-Figure 3.14

show the vertical velocity profile of the horizontally-averaged velocity measurements for each section of ADCP measurements, and they provide intuition about model fitness, measurement bounds, and performance of the velocity extrapolation. The upstream section shows good agreement with the model results from the channel bottom to the top of the measured section. The velocity extrapolated from the top of the measured section to the water surface diverges from the numerical solution and the apparent trend of the measured velocity. The river right section shows good agreement with the model results from the channel bottom to the bottom of the measured section, but there is rapid divergence from the numerical solution from the bottom of the measured velocity. The downstream section shows poor agreement with the model throughout the water column. The discrepancy between extrapolated velocity and modeled velocity approaches 1 m/s at the water surface. The river left section has a similar shape to the modeled velocity until the extrapolation from the top of the measured section to the water surface.

Figure 3.15 shows that imposing the SPH inlet condition based on the horizontally-averaged ADCP measurements for the upstream section leads to poor fitness with increasing proximity to the higher velocities attributed to faster flow near the center channel and the wake tail of the nearest upstream boom island. Figure 3.17 shows good agreement of the SPH model with the overall trend of the river-left measurements, but the modeled velocity is consistently higher than the observed velocity. Figure 3.17 shows that the downstream section has the most disagreement between measured and modeled velocities, with residuals on the order of 1 m/s on the river-right (low percent distance) side. Figure 3.18 shows some agreement between measured and modeled velocity in the river-left section, but the wavelength of the velocity increase associated with the lateral flow deflection is longer in the SPH model than in the ADCP measurements.

Statistical measures of dispersion and model fitness shown in Table 3.3 confirms that despite the similar spread of the measured and modeled data, the downstream section shows the most disagreement between measurements and model results. While the river-left section of the SPH model appears to most faithfully represent the ADCP measurements, the river-right section hosts the lowest error. The disagreement associated with the upstream section represents a failure of the laterally-uniform velocity inlet condition to simulate the variability of the natural system.

There are a litany of cases where SPH solvers, and DualSPHysics in particular, produce numerical results that compare very favorably with experimental data (e.g., Crespo et al., 2011; Gomez-Gesteira et al., 2012; Altomare et al., 2014; Crespo et al., 2017). The SPH simulations presented here use design parameters (e.g., artificial viscosity, kernel type, boundary condition treatment, time-stepping algorithm, and more) which are consistent with published values for simulations validated with experimental results. Disagreement between the ADCP measurements and SPH results is clearly due to simplifications in experimental design and does not represent a performance problem with the SPH method or the DualSPHysics code. In addition to model setup, significant simplification was made in the creation of SPH velocity transects to compare with the ADCP measurements. Creating numerical transects that undulate like the path of the ADCP transects shown in Figure 3.5 and Figure 3.6 is non-trivial, and the comparison of the ADCP transects to the simulation domain shown in Figure 3.7 is inherently uneven.

Bathymetric data will probably improve agreement between measurements and model results. A 1.9 m variability in channel bottom depth of the four measured sections matters in this case since the profiles have an average depth of only 2.35 m. Ideally, measurement of a solitary boom island unaffected by the wake of nearby boom islands would make for simpler comparison of measured and modeled velocities without needing to add much complexity to the model domain,

but boom islands tend to be closely clustered. To reconcile the presence of boom island clusters in the model domain, either a laterally variable inlet velocity should be introduced and/or the model domain should be lengthened to include upstream boom islands. The latter option is not only simpler to implement but could also help to determine if there is amplification or decay in the complexity and magnitude of channel velocity.

While there are details of the velocity measurements that are not simulated with precision by the simple SPH model, the similarity in the general flow pattern derived from computations is sufficient to rely on the SPH model for information about the effects of the boom island on the channel flow field. Figure 3.9 shows that the downstream influence of the boom island is strong until near the downstream end of its wake, after which point there is a steady reorganization of the velocity field. By the end of the length of the domain, the variability in velocity caused by the boom island is virtually zero. Channel velocity near the boom island does tend to increase overall, but there is simultaneous creation of velocity zones that are less than half of the inlet velocity extending for almost 30 m. These areas in the wake of the boom island could promote spawning habitat by providing velocity shelter for fishes when flows are high and may promote feeding and rearing habitat across separate or overlapping discharge ranges.

In terms of the velocity boundaries for shortnose sturgeon habitat suitability outlined by Johnston (2016), the SPH model indicates that the boom island does not create favorable spawning habitat during low flows such as experienced on June 4, 2018, when the ADCP measurements of the Veazie Impoundment Area were taken. Figure 3.10 shows that the boom island lowers velocity to a point that increases the risk of loss of shortnose sturgeon eggs to fungal growth and predation. Because the modeled velocity conditions are not representative of the spring flows considered in Johnston's HSI maps for the Veazie Impoundment Area, it would be useful to

determine a series of characteristic water surface elevations and associated surface velocities that are representative of typical spring flows. Refining the SPH model and running it at typical spring discharges would help to establish the lower and upper discharge limits for which boom islands serve as refugia for diadromous fishes as well as the effect of increased discharge on the horizontal extent of boom island influence on channel velocity.

In terms of broader impacts to aquatic habitat, the velocity heterogeneity provided by the deflection of flow by boom islands impacts species other than shortnose sturgeon, and the effects likely impact various species across various life stages. Investigations of the impacts of in-stream structures on various river-dwelling fish populations show that structures that add to habitat complexity tend to increase total fish abundance and biodiversity (e.g., Abbe and Montgomery, 1996; Pretty et al., 2003). Knowledge of preferred velocity conditions for shortnose sturgeon spawning supported by Johnston's research in the Veazie Impoundment Area provides a metric of habitat suitability which is directly related to an area which is densely-populated with boom islands. Further consideration of other fish species at various life stages will clarify the role of boom islands in the creation of aquatic habitat as a whole, strengthening the use of hydraulic modeling as a component of decision-making frameworks. To that end, resolving the impact of boom islands on the health of aquatic ecosystems will help to inform best practices surrounding the management of relict logging structures in river rehabilitation efforts.

The model results provide a useful lower bound for the spatial influence of a boom island on the local velocity field. Using the variance of the vertically-averaged velocity (Figure 3.9) as a metric of changed velocity field, the presence of a typical boom island in the Penobscot River appreciably changes the velocity structure for at least 40 m in the direction of mean flow. While the information resulting from the ADCP measurements and SPH modeling presented here is

limited to a single boom island at a single discharge value, the approach to this problem is scalable at multiple discharges and spatial scales. If the effects of a single boom island can be faithfully modeled, then modeling the cumulative effects of boom island clusters is a natural extension of this investigation.

Since clustered boom islands in the Veazie Impoundment Area are separated by an average of 48 m ($s = 27$ m), it is highly likely that there are cumulative effects to the downstream velocity structure, especially during high discharge. The obliquity of the boom islands with respect to the direction of mean channel flow coupled with the tendency of in-stream structures to produce von Kármán vortices during high-Re flows suggests that with increasing discharge, the lateral extent of the velocity field perturbation will become more pronounced. Although the wake shown in Figure 3.8 is stable at low flows, vortex shedding at high-Re flows will cause high-frequency changes in the lateral curvature of the velocity field perturbation. While the upper bounds of the spatial influence of a boom island or clusters of boom islands are still unknown, the low-discharge scenario modeled in this investigation contributes to decision-making tools by establishing that each boom island contributes to a velocity field perturbation for at least 40 m in the direction of mean channel flow. Ongoing efforts to measure channel velocity in a variety of flow conditions and refinement of the numerical model setup would help to conclusively determine the effects of relict logging infrastructure on channel velocity and habitat suitability for diadromous fishes.

WORKS CITED

Abbe, T.B., and Montgomery, D.R., 1996, LARGE WOODY DEBRIS JAMS, CHANNEL HYDRAULICS AND HABITAT FORMATION IN LARGE RIVERS: Regulated Rivers: Research & Management, v. 12, p. 201–221, doi: 10.1002/(SICI)1099-1646(199603)12:2/3<201::AID-RRR390>3.0.CO;2-A.

Altomare, C., Crespo, A.J.C., Rogers, B.D., Dominguez, J.M., Gironella, X., and Gómez-Gesteira, M., 2014, Numerical modelling of armour block sea breakwater with smoothed particle hydrodynamics: Computers and Structures, v. 130, p. 34–45, doi: 10.1016/j.compstruc.2013.10.011.

Arneson, L. a., Zevenbergen, L.W., Lagasse, P.F., and Clopper, P.E., 2012, Evaluating Scour at Bridges: U.S. Department of Transportation Federal Highway Administration, doi: 10.1016/S0021-9797(02)00157-1.

Barreiro, A., Crespo, A.J.C., Domínguez, J.M., and Gómez-Gesteira, M., 2013, Smoothed Particle Hydrodynamics for coastal engineering problems: Computers and Structures, v. 120, p. 96–106, doi: 10.1016/j.compstruc.2013.02.010.

Boavida, I., Santos, J.M., Cortes, R. V., Pinheiro, A.N., and Ferreira, M.T., 2011, Assessment of instream structures for habitat improvement for two critically endangered fish species: Aquatic Ecology, v. 45, p. 113–124, doi: 10.1007/s10452-010-9340-x.

Bollaert, E., and Schleiss, A., 2003, Scour of rock due to the impact of plunging high velocity jets Part I: A state-of-the-art review: Journal of Hydraulic Research, v. 41, p. 451–464, doi: 10.1080/00221680309499991.

Brasington, J., and Richards, K., 2007, Reduced-complexity, physically-based geomorphological modelling for catchment and river management: Geomorphology, v. 90, p. 171–177, doi: 10.1016/j.geomorph.2006.10.028.

Brito, M., Canelas, R.B., and Ferreira, R.M.L., 2016, Coupling between DualSPHysics and Chrono- Engine : towards large scale HPC multiphysics simulations: 11th International SPHERIC Workshop, p. 6–7.

Canelas, R.B., Brito, M., Feal, O.G., Domínguez, J.M., and Crespo, A.J.C., 2018, Extending DualSPHysics with a Differential Variational Inequality: modeling fluid-mechanism interaction: Applied Ocean Research, v. 76, p. 88–97, doi: 10.1016/j.apor.2018.04.015.

Canelas, R.B., Crespo, A.J.C., Domínguez, J.M., Ferreira, R.M.L., and Gómez-Gesteira, M., 2016, SPH-DCDEM model for arbitrary geometries in free surface solid-fluid flows: Computer Physics Communications, v. 202, p. 131–140, doi: 10.1016/j.cpc.2016.01.006.

Canelas, R.B., Domínguez, J.M., Crespo, A.J.C., Gómez-Gesteira, M., and Ferreira, R.M.L., 2017, Resolved Simulation of a Granular-Fluid Flow with a Coupled SPH-DCDEM Model: Journal of Hydraulic Engineering, v. 143, p. 06017012, doi: 10.1061/(ASCE)HY.1943-7900.0001331.

Carretier, S., Martinod, P., Reich, M., and Godderis, Y., 2016, Modelling sediment clasts transport during landscape evolution: Earth Surface Dynamics, v. 4, p. 237–251, doi: 10.5194/esurf-4-237-2016.

Crespo, A.J.C., Altomare, C., Domínguez, J.M., González-Cao, J., and Gómez-Gesteira, M., 2017, Towards simulating floating offshore oscillating water column converters with Smoothed Particle Hydrodynamics: Coastal Engineering, doi: 10.1016/j.coastaleng.2017.05.001.

Crespo, A.C., Dominguez, J.M., Barreiro, A., Gómez-Gesteira, M., and Rogers, B.D., 2011, GPUs, a new tool of acceleration in CFD: Efficiency and reliability on smoothed particle hydrodynamics methods: PLoS ONE, v. 6, doi: 10.1371/journal.pone.0020685.

Crespo, A.J.C., Domínguez, J.M., Rogers, B.D., Gómez-Gesteira, M., Longshaw, S., Canelas, R., Vacondio, R., Barreiro, A., and García-Feal, O., 2015, DualSPHysics: Open-source parallel CFD solver based on Smoothed Particle Hydrodynamics (SPH): Computer Physics Communications, v. 187, p. 204–216, doi: 10.1016/j.cpc.2014.10.004.

Crespo, A.J.C., Gómez-Gesteira, M., and Dalrymple, R.A., 2007, Boundary conditions generated by dynamic particles in SPH methods: Computers, Materials and Continua, v. 5, p. 173–184, doi: 10.3970/cmc.2007.005.173.

Croissant, T., and Braun, J., 2014, Constraining the stream power law: a novel approach combining a landscape evolution model and an inversion method: Earth Surface Dynamics, v. 2, p. 155–166, doi: 10.5194/esurf-2-155-2014.

D'Errico, J., 2012, inpaint_nans:, https://www.mathworks.com/matlabcentral/fileexchange/4551-inpaint_nans.

Dubinski, I.M., and Wohl, E., 2013, Relationships between block quarrying, bed shear stress, and stream power: A physical model of block quarrying of a jointed bedrock channel: Geomorphology, v. 180–181, p. 66–81, doi: 10.1016/j.geomorph.2012.09.007.

Fourtakas, G., and Rogers, B.D., 2016, Modelling multi-phase liquid-sediment scour and resuspension induced by rapid flows using Smoothed Particle Hydrodynamics (SPH) accelerated with a Graphics Processing Unit (GPU): Advances in Water Resources, v. 92, p. 186–199, doi: 10.1016/j.advwatres.2016.04.009.

George, M., Sitar, N., and Sklar, L.S., 2015, Experimental Evaluation of Rock Erosion in Spillway Channels: American Rock Mechanics Association, p. 1–6.

Gomez-Gesteira, M., Crespo, A.J.C.J.C., Rogers, B.D.D., Dalrymple, R.A.A., Dominguez, J.M.M., and Barreiro, A., 2012, SPHysics - development of a free-surface fluid solver - Part 2: Efficiency and test cases: Computers and Geosciences, v. 48, p. 300–307, doi: 10.1016/j.cageo.2012.02.028.

Haro, A., Chelminski, M., and Dudley, R.W., 2015, Computational Fluid Dynamics-Habitat Suitability Index (CFD-HSI) Modelling as an Exploratory Tool for Assessing Passability of Riverine Migratory Challenge Zones for Fish.: River Research & Applications, v. 31, p. 526–537, doi: 10.1002/rra.2911.

Hooke, R.L.B., Hanson, P.R., Belknap, D.F., and Kelley, A.R., 2017, Late glacial and Holocene history of the Penobscot River in the Penobscot Lowland, Maine: Holocene, v. 27, p. 726–739, doi: 10.1177/0959683616670474.

Howard, A.D., 1994, A detachment-limited model of drainage basin evolution: Water Resources Research, v. 30, p. 2261–2285, doi: 10.1029/94WR00757.

Howard, A.D., and Kerby, G., 1983, Channel changes in badlands: Geological Society of America Bulletin, v. 94, p. 739–752, doi: 10.1130/0016-7606(1983)94<739:CCIB>2.0.CO;2.

Inc., I.C.G., 2017, FLAC3D — Fast Lagrangian Analysis of Continua in Three-Dimensions:

Istanbulluoglu, E., Tarboton, D.G., Pack, R.T., and Luce, C., 2003, A sediment transport model for incision of gullies on steep topography: Water Resources Research, v. 39, p. 1–15, doi: 10.1029/2002WR001467.

Johnston, C.K., 2016, SHORTNOSE STURGEON (ACIPENSER BREVIROSTRUM) SPAWNING POTENTIAL IN THE PENOBSCOT RIVER, MAINE: CONSIDERING DAM REMOVALS AND EMERGING THREATS: University of Maine, 109 p.

Joyce, T.M., 1989, On In Situ “Calibration” of Shipboard ADCPs: Journal of Atmospheric and Oceanic Technology, doi: 10.1175/1520-0426(1989)006<0169:OISOSA>2.0.CO;2.

von Kármán, T., 1930, Mechanische Ähnlichkeit und Turbulenz: Nachr. Ges. Wiss. Math-Phys Klasse Göttingen, v. 5, p. 58–76, doi: 10.1111/j.1365-2966.2005.09427.x.

Koons, P., and Upton, P. The Failure Earth Response Model:

Lamb, M.P., Finnegan, N.J., Scheingross, J.S., and Sklar, L.S., 2015, New insights into the mechanics of fluvial bedrock erosion through flume experiments and theory: Geomorphology, v. 244, p. 33–55, doi: 10.1016/j.geomorph.2015.03.003.

Lamb, M.P., and Fonstad, M.A., 2010, Rapid formation of a modern bedrock canyon by a single flood event: Nature Geoscience, v. 3, p. 477–481, doi: 10.1038/ngeo894.

Liao, C.-T., Yeh, K.-C., and Huang, M.-W., 2014, Development and application of 2-D mobile-bed model with bedrock river evolution mechanism: Journal of Hydro-environment Research, v. 8, p. 210–222, doi: 10.1016/j.jher.2013.03.001.

Mazhar, H., Heyn, T., Pazouki, A., Melanz, D., Seidl, A., Bartholomew, A., Tasora, A., and Negrut, D., 2013, CHRONO: A parallel multi-physics library for rigid-body, flexible-body, and fluid dynamics: Mechanical Sciences, v. 4, p. 49–64, doi: 10.5194/ms-4-49-2013.

Monaghan, J.J., 2005, Smoothed particle hydrodynamics: Reports on Progress in Physics, v. 68, p. 1703–1759, doi: 10.1088/0034-4885/68/8/R01.

Opperman, J.J., Royte, J., Banks, J., Day, L.R., and Apse, C., 2011, The Penobscot River, Maine, USA: A basin-scale approach to balancing power generation and ecosystem restoration: Ecology and Society, doi: 10.5751/ES-04117-160307.

Pretty, J.L., Harrison, S.S.C., Shepherd, D.J., Smith, C., Hildrew, A.G., and Hey, R.D., 2003, River rehabilitation and fish populations: assessing the benefit of instream structures: Journal of Applied Ecology, v. 40, p. 251–265, doi: 10.1046/j.1365-2664.2003.00808.x.

Roni, P., Beechie, T., Pess, G., and Hanson, K., 2015, Wood placement in river restoration: fact, fiction, and future direction (B. Jonsson, Ed.): Canadian Journal of Fisheries and Aquatic Sciences, v. 72, p. 466–478, doi: 10.1139/cjfas-2014-0344.

Roy, S.G., Koons, P.O., Upton, P., and Tucker, G.E., 2016, Dynamic links among rock damage, erosion, and strain during orogenesis: Geology, v. 44, p. 583–586, doi: 10.1130/G37753.1.

Roy, S.G., Koons, P.O., Upton, P., and Tucker, G.E., 2015, The influence of crustal strength fields on the patterns and rates of fluvial incision: Journal of Geophysical Research: Earth Surface, v. 120, p. 275–299, doi: 10.1002/2014JF003281.

Scheingross, J.S., and Lamb, M.P., 2017, A Mechanistic Model of Waterfall Plunge Pool Erosion into Bedrock: Journal of Geophysical Research: Earth Surface, v. 122, p. 2079–2104, doi: 10.1002/2017JF004195.

Shobe, C.M., Tucker, G.E., and Anderson, R.S., 2016, Hillslope-derived blocks retard river incision: Geophysical Research Letters, v. 43, p. 5070–5078, doi: 10.1002/2016GL069262.

Steffler, P., and Blackburn, J., 2002, River2D: Two-dimensional Depth-averaged Model of River Hydrodynamics and Fish Habitats. University of Alberta, Edmonton, Canada.:

Tafuni, A., Domínguez, J.M., Vacondio, R., and Crespo, A.J.C., 2018, A versatile algorithm for the treatment of open boundary conditions in Smoothed particle hydrodynamics GPU models: Computer Methods in Applied Mechanics and Engineering, v. 342, p. 604–624, doi: 10.1016/j.cma.2018.08.004.

Temme, A.J.A.M., Armitage, J., Attal, M., van Gorp, W., Coulthard, T.J., and Schoorl, J.M., 2017, Developing, choosing and using landscape evolution models to inform field-based landscape reconstruction studies: Earth Surface Processes and Landforms, v. 42, p. 2167–2183, doi: 10.1002/esp.4162.

Tucker, G.E., and Hancock, G.R., 2010, Modelling landscape evolution: Earth Surface Processes and Landforms, v. 35, p. 28–50, doi: 10.1002/esp.1952.

US Army Corps of Engineers, 2016, HEC-RAS River Analysis System: Hydraulic Reference Manual:

Whipple, K.X., DiBiase, R.A., and Crosby, B.T., 2013, Bedrock Rivers, *in* Treatise on Geomorphology, v. 9, doi: 10.1016/B978-0-12-374739-6.00254-2.

Whipple, K.X., Hancock, G.S., and Anderson, R.S., 2000, River incision into bedrock: Mechanics and relative efficacy of plucking, abrasion, and cavitation: GSA Bulletin, v. 112, p. 490–503.

Whipple, K.X., and Tucker, G.E., 1999, Dynamics of the stream-power river incision model: Implications for height limits of mountain ranges, landscape response timescales, and research needs: Journal of Geophysical Research: Solid Earth, v. 104, p. 17661–17674, doi: 10.1029/1999JB900120.

Wilcock, P.R., 1996, Estimating Local Bed Shear Stress from Velocity Observations: Water Resources Research, v. 32, p. 3361–3366, doi: 10.1029/96WR02277.

Zubeldia, E.H., Fourtakas, G., Rogers, B.D., and Farias, M.M., 2018, Multi-phase SPH model for simulation of erosion and scouring by means of the shields and Drucker–Prager criteria.: Advances in Water Resources, v. 117, p. 98–114, doi: 10.1016/j.advwatres.2018.04.011.

APPENDICES

Appendix A: CHAPTER 2

Below is the Python code used to drive erosion in the FLAC3D implementation of the Failure Earth Response Model (FERM).

```
import itasca as it
import matplotlib.pyplot as plt
import time
it.command("python-reset-state false")

delta_z = it.fish.get("delta_z")
xmin = it.fish.get("xmin")
xmax = it.fish.get("xmax")
ymin = it.fish.get("ymin")
ymax = it.fish.get("ymax")


########################################################################
# DEFINE THE FUNCTIONS USED TO DRIVE THE FAILURE EARTH RESPONSE MODEL #
########################################################################

def getSurface():
### Set zones to "ZonesAtSurface" and associated gridpoints to "GpAtSurface" ###
### if they are in the ZonesAtSurface group and are not null zones. ###
  ZonesAtSurface = set()
  GpAtSurface = set()
  for pnt in it.zone.list():
    if (pnt.in_group("ZonesAtSurface") == True) and (pnt.model != "null"):
      ZonesAtSurface.add(pnt.id())
      for gpt in pnt.gridpoints():
        GpAtSurface.add(gpt.id())
        initializeGpExtra(gpt)
  return ZonesAtSurface, GpAtSurface
```

```
def testFailure(pnt):
### Test to see if the zone is in failure (shear or tensile) ###
  current_state = pnt.state(False)
  pnt.set_extra(4, current_state)
  zone_extra_1 = pnt.extra(1)
  zone_extra_2 = pnt.extra(2)
  if (current_state in {1,3,5,7,9,11,13,15}) and (zone_extra_1 < 1):
    # shear failure now or in past
    pnt.set_extra(1,(zone_extra_1 + 1))
  if current_state in {2,3,6,10,11,14,15} and (zone_extra_2 < 1):
    # tensile failure not or in past
    pnt.set_extra(2,(zone_extra_2 + 1))
  inFailure = ( pnt.extra(1) | pnt.extra(2) >= 1 ) # evaluates to 'True' or 'False'
  return inFailure



def initializeGpExtra(gpt):

  try:
    [gpt.extra(i) for i in (2,3,4)] # test to see if forces are stored
                                    # in gp_extra slots 2-4
  except AssertionError:
    [gpt.set_extra(i,0) for i in (2,3,4)] # initialize gp_extra slots
                                          # 1-3 if no gp_extra has been assigned



def addZonesAtSurface(pnt):

### Add a new zone to the set of surface zones ###

  pnt.set_group("ZonesAtSurface","default") # add zone to ZonesAtSurface group
  ZonesAtSurface.add(pnt.id())
  for gpt in pnt.gridpoints():
    GpAtSurface.add(gpt.id())
    initializeGpExtra(gpt)
```

```
def getNeighbours(pnt):
### Return a dictionary of zones which are attached to the gridpoints of zone pnt ###
  neighbours = {str(zn.id()):zn for gpt in pnt.gridpoints() for zn in gpt.zones() if zn.id()
!= pnt.id()}
  return neighbours
  # Note that getNeighbours(pnt) is a dictionary comprehension & an optimized version of
  # the below for loop, included here for clarity:
  #
  #  neighbours = {}
  #  for gpt in pnt.gridpoints():
  #    for zn in gpt.zones():
  #      if zn.id() != pnt.id():
  #        znID = str(zn.id())
  #        neighbours[znID] = zn



def findLowerNeighbours(pnt):
### Perform a search of the nearest neighbours and return a dictionary of zones
### which have an elevation lower than that of pnt
  lowerNeighbours = {}
  elevation_pnt = pnt.pos_z()
  neighbours = getNeighbours(pnt)
  for nz in neighbours.values():
    if (nz.in_group("ZonesAtSurface") == True) and (nz.model != "null"):
      elevation_nz = nz.pos_z()
      if ((elevation_nz + delta_z) < elevation_pnt):
        nzID = str(nz.id())
        lowerNeighbours[nzID] = nz
  return lowerNeighbours
```

```
def testTransportable(pnt, fluvialTransport=False):

### Search for lower zones within the nearest neighbours of the zone's nearest ###
### neighbours. Optionally, use a fluvial transport condition which will evacuate ###
### a zone in failure so long as it has non-zero forces in the flow-parallel ###
### direction. ###
### EXAMPLE 1: testTransportable(pnt) ###
### EXAMPLE 2: testTransportable(pnt, fluvialTransport=True) ###
  isTransportable = False
  if (fluvialTransport == True):
    try:
      fluvialTransport = any([(abs(gpt.extra(2))) > 0 for gpt in pnt.gridpoints()])
    except AssertionError:
      pass
    # returns True if any flow-parallel forces are present, False if not
  firstNeighbours = findLowerNeighbours(pnt)
    # returns a lowerNeighbours dictionary for pnt
  secondNeighbours = ()
  if bool(firstNeighbours): # if the firstNeighbours dictionary isn't empty...
    for nz in firstNeighbours.values(): # for each neighbour zone...
      secondNeighbours = findLowerNeighbours(nz)
        # ...return a new lowerNeighbours dictionary
  if (len(secondNeighbours) >= 1):
    # if at least one zone in the second neighbourhood is lower than pnt
    isTransportable = True
  elif fluvialTransport == True:
    isTransportable = True
  else:
    isTransportable = False
  return isTransportable
```

```
def checkNeighboursAtSurface(pnt):
### Test to see if neighbouring zones aren't in the ZonesAtSurface group
### and should be. A surface zone is defined by having a face created by
### vertices connected to fewer than 8 other zones. ###
### As long as the second input argument isn't "false" then the zone will
### be added to the ZonesAtSurface group and associated set if it is
### determined to be at the surface. ###
  neighbours = getNeighbours(pnt)
  for nz in neighbours.values():
    if (nz is not None) and (nz.in_group("ZonesAtSurface") == False) and
(nz.in_group("boundary") == False):
      for face in nz.faces(): # loop through all faces in zone
        surface_check = 0
        for gp in face: # count the number of zones connected to the gp
          z_model = [z.model() for z in gp.zones()]
          zone_connections = ( len(z_model) - z_model.count('null') )
            # count number of non-null zones connected to the gp
          if (zone_connections < 8):
            surface_check += 1
        if (surface_check == 4):
          # if all vertices in the face are connected to fewer than 8 other zones
          if ((xmin < nz.pos_x() < xmax) and (ymin < nz.pos_y() < ymax)):
            addZonesAtSurface(nz)
```

```
def findZoneBelow(pnt):
### Find zone below by first searching for a zone which shares the lower ###
### face of the zone in question. If no zone shares the lower face, search ###
### for zones below by decrementing by delta_z ###
  pnt_adjacent = pnt.adjacent_zones()
  if pnt_adjacent[0] is not None:
    pnt_below = pnt_adjacent[0]
  else:
    zpos_below = pnt.pos_z() - delta_z
    try:
      pnt_below = it.zone.near((pnt.pos_x(),pnt.pos_y(),zpos_below))
    except:
      valid_zone = False
      zpos_attempt_count = 0
      while valid_zone == False:
        zpos_below -= delta_z
          # keep decretmenting zpos_below until a valid zone is found
        zpos_attempt_count += 1
        if zpos_attempt_count < 5:
          try:
            pnt_below = it.zone.near((pnt.pos_x(),pnt.pos_y(),zpos_below))
            valid_zone = True
          except:
            pass # give up looking if there are no zones 5 delta_z units below
  return pnt_below




def testFloating(pnt):
  zoneFloating = True
  for gpt in pnt.gridpoints():
    z_model = [z.model() for z in gpt.zones()]
    zone_connections = ( len(z_model) - z_model.count('null') )
      # count number of non-null zones connected to the gp
    if (zone_connections > 1):
      zoneFloating = False
  return zoneFloating
```

```
def copyGpExtra(pnt1, pnt2, slots):
### Let the new zone inherit the old zone's data stored in gp_extra slots
### (SPH forces, etc.)
  for (gpt1,gpt2) in zip(pnt1.gridpoints(),pnt2.gridpoints()):
    if (type(slots) is tuple):
      [gpt2.set_extra(slot,gpt1.extra(slot)) for slot in slots]
    elif (type(slots) is int):
      gpt2.set_extra(slots,gpt1.extra(slots))
    else:
      raise ValueError('The copyGpExtra function expects either a single integer slot number
or a tuple of slot numbers.')




def removeZones(ZonesAtSurface, GpAtSurface, ZonesToRemove):
### Remove to the set of surface zones ###
  GpToRemove = set()
  for pnt_id in ZonesToRemove:
    pnt = it.zone.find(pnt_id)
    pnt.set_model("null")
    checkNeighboursAtSurface(pnt)
    for gpt in pnt.gridpoints():
      if (not any([zn.in_group("ZonesAtSurface") for zn in gpt.zones()])):
        GpToRemove.add(gpt.id())
    ZonesAtSurface.remove(pnt_id) # remove the nulled zone from ZonesAtSurface
    it.fish.set("count_total_erosion", (it.fish.get("count_total_erosion") + 1))
  [GpAtSurface.remove(gp_id) for gp_id in GpToRemove]
  return ZonesAtSurface, GpAtSurface
```

```
def addZones(ZonesAtSurface, GpAtSurface, ZonesToAdd):
### Add new zones to the set of surface zones (ZonesAtSurface) ###
  for pnt_id in ZonesToAdd:
    pnt = it.zone.find(pnt_id)
    pnt.set_group("ZonesAtSurface","default") # add zone to ZonesAtSurface group
    ZonesAtSurface.add(pnt_id)
    for gpt in pnt.gridpoints():
      GpAtSurface.add(gpt.id())
      gpt.set_extra(1,gpt.pos_z())
      initializeGpExtra(gpt)
  return ZonesAtSurface, GpAtSurface
def zoneBelowSetProperty(pnt, layersDown, groupName=None, cohesion=None, tension=None,
friction=None):
### Set the group of the zone below pnt for a given number of layers ###
### below the surface ###
  for i in range (1,layersDown):
    pnt_adjacent = pnt.adjacent_zones()
    pnt_below = pnt_adjacent[0]
    if groupName is not None:
      pnt_below.set_group(groupName,"2")
    if cohesion is not None:
      pnt_below.set_prop('cohesion',cohesion)
    if tension is not None:
      pnt_below.set_prop('tension',tension)
    if friction is not None:
      pnt_below.set_prop('friction',friction)
    pnt = pnt_below



def makeUnconsolidated(ZonesAtSurface, layersDown=1):
### Make the zones at the surface (and layers underneath) unconsolidated ###
### material. Set layersDown to 1 to only make the uppermost layer ###
### (ZonesAtSurface) unconsolidated. ###
  for pnt_id in ZonesAtSurface:
    pnt = it.zone.find(pnt_id)
    pnt.set_group("Unconsolidated","2")
    pnt.set_prop('cohesion',1e3)
    pnt.set_prop('tension',1e2)
    pnt.set_prop('friction',5)
    if layersDown > 1:
      zoneBelowSetProperty(pnt, layersDown, groupName="Unconsolidated", cohesion=1e3,
tension=1e2, friction=5)
```

```
def addFluidPressure(method='hydrostatic'):
### Initialise pore pressure based on hydrostatic pressure. ###
### OPTIONAL: add pore pressure to surface zones as a function of wetting ###
### by hydraulics (SPH). ###
### EXAMPLE 1: addFluidPressure()
### EXAMPLE 2: addFluidPressure(method='hydraulic')
  for gpt in it.gridpoint.list():
    pnt_count = 0
    pnt_pp_total = 0
    for pnt in gpt.zones(): # for all zones attached to the gridpoint...
      atmospheric = False
      pnt_adjacent = pnt.adjacent_zones()
      pnt_above = pnt_adjacent[1]
      if pnt_above is None:
        pnt_above = pnt
      if (pnt.in_group("ZonesAtSurface") == True) or (pnt_above.in_group("ZonesAtSurface")
== True):
        atmospheric = True
        break
      pnt_pp = pnt.density() * it.gravity_z() * pnt.pos_z()
      pnt_pp_total += pnt_pp
      pnt_count += 1
    if atmospheric == True:
      gpt.set_pp(0)
    else:
      gpt_pp = pnt_pp_total / pnt_count
      gpt.set_pp(gpt_pp)
  if ('hydraulic' in method):
    for gpt in GpAtSurface:
      gpt = it.gridpoint.find(gpt)
      try:
        if (abs(gpt.extra(2) + gpt.extra(3) + gpt.extra(4)) > 0):
          # if XYZ forces have been applied (via SPH, etc.)...
          gpt.set_pp( gpt.pp() + (abs(gpt.extra(4))/(0.05)) )
      except AssertionError:
        pass # move on if gp_extra hasn't been defined for that gp's slots 2-4 yet
```

```
def erosion(ZonesAtSurface, GpAtSurface):
### Drive the erosion process by managing the removal of zones in failure
  ZonesToAdd = set()
  ZonesToRemove = set()
  it.fish.call_function("StrengthStressRatio") # store the Stress-Strength Ratio in
    # z_extra(10) using a fish function
  for pnt_id in ZonesAtSurface:
    pnt = it.zone.find(pnt_id)
    zoneExtras(pnt)
    if (testFailure(pnt) == testTransportable(pnt, fluvialTransport=True) == True):
      # if the zone is both in failure and transportable...
      ZonesToRemove.add(pnt_id) # mark the zone for removal
      erosion_step = it.cycle()
      pnt_below = findZoneBelow(pnt)
      if (pnt_below.model != "null"):
        ZonesToAdd.add(pnt_below.id())
        zoneExtras(pnt_below)
        pnt_below.set_extra(5,1)
        copyGpExtra(pnt, pnt_below, (2,3,4)) # copy forces stored in gp_extra slots 2-4
  NumberZonesEroded = len(ZonesToRemove)
  ZonesAtSurface, GpAtSurface = removeZones(ZonesAtSurface, GpAtSurface, ZonesToRemove)
  ZonesAtSurface, GpAtSurface = addZones(ZonesAtSurface, GpAtSurface, ZonesToAdd)
  ZonesToAdd.clear()
  ZonesToRemove.clear()
  return NumberZonesEroded
```

```
#######################################
# CALL THE FUNCTIONS TO DRIVE EROSION #
#######################################
ZonesAtSurface, GpAtSurface = getSurface()
addFluidPressure(method='hydraulic')
makeUnconsolidated(ZonesAtSurface, layersDown=2)
StartingTimestep = it.cycle()
TotalZonesEroded = 0
PlotSteps = 0
ErosionRecord = {}
ErosionRateRecord = {}
fig = plt.figure()
ax1 = fig.add_subplot(2, 1, 1)
ax2 = fig.add_subplot(2, 1, 2)
plt.show()
plt.subplot(2, 1, 1)
plt.title('FERM Erosion')
plt.ylabel('Total Erosion (zones)')
plt.subplot(2, 1, 2)
plt.xlabel('timestep')
plt.ylabel('Erosion Rate (zones/step)')



def plot_erosion_rate(fig, ErosionRecord, ErosionRateRecord):
  x1 = ErosionRecord.keys()
  y1 = ErosionRecord.values()
  x2 = ErosionRateRecord.keys()
  y2 = ErosionRateRecord.values()
  plt.subplot(2, 1, 1)
  plt.plot(x1, y1, 'k.-')
  plt.subplot(2, 1, 2)
  plt.plot(x2, y2, 'b.-')
  fig.canvas.draw()
  fig.canvas.flush_events()
```

```
def erosion_callback(*args):
  global TotalZonesEroded
  global ErosionRecord
  global StartingTimestep
  global ErosionRecord
  global ErosionRateRecord
  global fig
  start_time = time.time()
  NumberZonesEroded = erosion(ZonesAtSurface, GpAtSurface)
  it.fish.set('ZonesEroded',NumberZonesEroded)
  timestep = it.cycle() - StartingTimestep
  TotalZonesEroded = TotalZonesEroded + NumberZonesEroded
  ErosionRecord[timestep] = TotalZonesEroded
  ErosionRateRecord[timestep] = NumberZonesEroded
  plot_erosion_rate(fig, ErosionRecord, ErosionRateRecord)
  print("--- Erosion cycle runtime: %.1f seconds || Zones eroded: %s || Total eroded zones:
%s ---" % ( (time.time() - start_time), NumberZonesEroded, TotalZonesEroded) + '\n')

it.remove_callback("erosion_callback",-1)
  # remove any lingering callback to the erosion function
it.set_callback("erosion_callback", -1)
  # use [ it.remove_callback("erosion_callback",-1) ]
  # to stop Python erosion functions during cycling
```

Appendix B: CHAPTER 3

Figure C3.1 –Map of the ADCP Transect Across the Veazie Impoundment

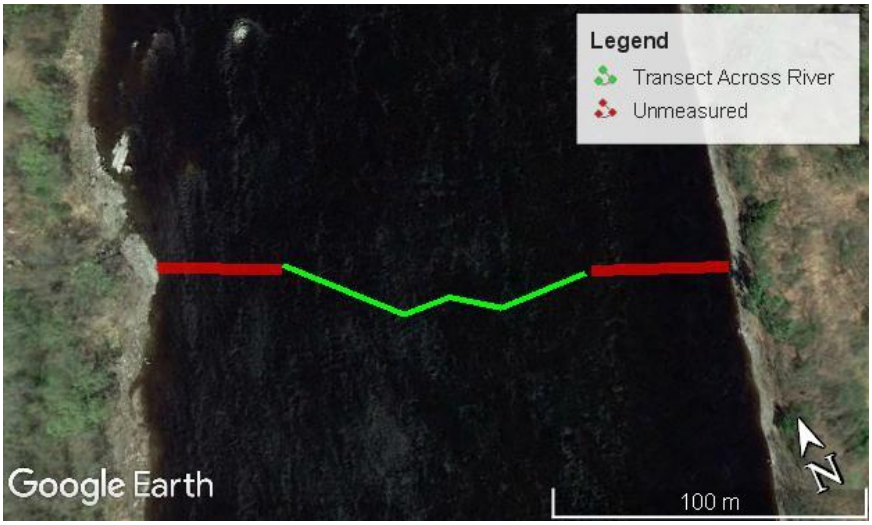

Discharge estimates were made with the assumption that the shallow, unnavigable lateral boundaries of the measured transect account for 15% of the flow.

BIOGRAPHY OF THE AUTHOR

Nick Richmond was born in London, UK and was raised on Mount Desert Island, Maine before moving to Yarmouth, Maine. He graduated from Yarmouth High School in 2007 and attended Vassar College and Southern Maine Community College before transferring to University of Maine in 2013. His interest in geophysics and numerical modeling led to an undergraduate research position in the Geodynamics Numerical Modeling Facility in the School of Earth and Climate Sciences. After graduating with a BS in Earth Sciences from University of Maine in December 2015, he returned weeks later to begin his graduate studies in the School of Earth and Climate Sciences. In his spare time, Nick enjoys JAMstack web development, hang gliding, and baking bread. He is a candidate for the Master of Science degree in Earth and Climate Sciences from the University of Maine in December 2018.